



HAL
open science

Impact assessment of legacy wastes from ancient mining activities on current earthworm community

Anne-Lise Mariet, Honorine Gauthier-Manuel, Tiffany Lagiewski, Carole Bégeot, Anne-Véronique Walter-Simonnet, Frédéric Gimbert

► To cite this version:

Anne-Lise Mariet, Honorine Gauthier-Manuel, Tiffany Lagiewski, Carole Bégeot, Anne-Véronique Walter-Simonnet, et al.. Impact assessment of legacy wastes from ancient mining activities on current earthworm community. *Journal of Hazardous Materials*, 2020, 393 (10), pp.122369. 10.1016/j.jhazmat.2020.122369 . hal-02930050

HAL Id: hal-02930050

<https://hal.inrae.fr/hal-02930050>

Submitted on 22 Aug 2022

HAL is a multi-disciplinary open access archive for the deposit and dissemination of scientific research documents, whether they are published or not. The documents may come from teaching and research institutions in France or abroad, or from public or private research centers.

L'archive ouverte pluridisciplinaire **HAL**, est destinée au dépôt et à la diffusion de documents scientifiques de niveau recherche, publiés ou non, émanant des établissements d'enseignement et de recherche français ou étrangers, des laboratoires publics ou privés.



Distributed under a Creative Commons Attribution - NonCommercial 4.0 International License

1 **Impact assessment of legacy wastes from ancient mining activities on current earthworm**
2 **community**

3 Anne-Lise Mariet, Honorine Gauthier-Manuel, Tiffany Lagiewski, Carole Bégeot, Anne-
4 Véronique Walter-Simonnet, Frédéric Gimbert*

5

6 *Department of Chrono-Environment, University of Bourgogne Franche-Comté, UMR*
7 *UFC/CNRS 6249 USC INRA, 16 route de Gray, F-25030 Besançon Cedex, France*

8

9

10

11

12

13

14

15 *Corresponding author:

16 Frédéric Gimbert

17 Tel.: +33 (0) 381 665 775

18 Fax: +33 (0) 381 665 797

19 E-mail address: frederic.gimbert@univ-fcomte.fr

20 **Abstract**

21 Mineral resource exploitation by human societies throughout history led to the deposit
22 of mining and smelting wastes and the subsequent contamination of surrounding soils by trace
23 metals. After several centuries, the impact of these legacy hazardous wastes may remain a cause
24 of environmental concern, especially for indigenous soil invertebrate populations such as
25 earthworms. Therefore, we conducted a passive biomonitoring campaign in a former
26 metallurgical district (Vosges Mountains, eastern France). According to community
27 descriptors, we evidenced a significant decrease of anecic and endogeic earthworm density in
28 the former mining stations. To link these results to soil contamination and bioaccumulation
29 levels in earthworm tissues, we propose an original modelling approach using nonlinear mixed-
30 effects regression models. Beyond a dose-response relationship between metal internal
31 concentrations and their levels in soils, we highlighted contrasted behaviors according to
32 ecological groups (epianecics and endogeics most impacted). We interpreted these results in
33 relation to some eco-physiological features without completely exclude the influence of textural
34 characteristics of soil, especially for deep-burrowing species such as anecic strict. Nonetheless,
35 the presence of earthworm populations currently living in highly contaminated sites and
36 handling elevated internal concentrations raises the question of the acquisition of genetic
37 adaptive traits and the trophic transfers of metals.

38

39

40 **Keywords:** trace metal; bioaccumulation; density; soil fauna; ecological group

41

42 **1- Introduction**

43 Throughout history, mining and smelting activities of metals such as iron (Fe), copper
44 (Cu), lead (Pb), or silver (Ag) have played a leading role in the socio-economic development
45 of human societies (Tylecote, 1987). However, at the same time, they generated significant
46 amounts of potentially contaminated wastes whose weathering led to the release of trace metals
47 (TMs) in the environment. In Europe, the former mining district of Sainte-Marie-aux-Mines
48 (Vosges Mountains, eastern France) is known for its metal exploitation over the last millennium
49 and especially Pb and Ag during the 15th-16th centuries (Fluck, 2006). In this particular district,
50 it is estimated that more than 10% of the area is nowadays covered by several types of
51 metallurgical wastes, i.e., ore dumps, slags, and ore-washing sediments (Fluck, 2000; Mariet et
52 al., 2014). Persisting just a few centimeters deep, they affect both the physical (structure,
53 texture) and chemical properties of current soils. For instance, the contamination by TMs is
54 very elevated (up to several tens of thousands of mg_{Pb} kg⁻¹ soil) and still highly available for
55 potential transfers (Mariet et al., 2017b). Hence, using an active biomonitoring approach with
56 the land snail *Cantareus aspersus*, it has been recently demonstrated that TMs from medieval
57 mining activities (Pb-Ag extraction) were still bioavailable for this soil invertebrate (Mariet et
58 al., 2016) and represent a risk for environmental health (Mariet et al., 2017a). But what about
59 the current impacts of this legacy contaminated wastes on invertebrate populations living
60 locally on these sites? To answer this question, we conducted a passive bioindication campaign
61 in the former mining district of Sainte-Marie-aux-Mines by sampling earthworms at forested
62 stations subjected to different mining operations and presenting a contamination gradient.

63 As key organisms of soil functioning, earthworms are well recognized as good
64 indicators of environmental quality since they respond to a variety of environmental and
65 ecological factors such as changes in soil use and contamination (Pérès et al., 2011; Tondoh et
66 al., 2007). Moreover, although abundance is a classical endpoint for the assessment of

67 earthworm community responses to environmental stress, ecological structure (i.e., the
68 proportion of three main morpho-ecological groups: epigeic, endogeic and anecic) seems to be
69 a more sensitive indicator of soil pollution. Indeed, Pérès et al. (2011) showed that soil
70 contamination by PAHs and metals in industrial wastelands did not lead to a modification of
71 earthworm abundance although the ecological structure was strongly impacted. In the same
72 line, Nahmani et al. (2003) found, in soils from a former zinc smelter complex, a global
73 reduction of earthworm densities in relation with an eradication of endogeic species and a
74 reduction of epigeics.

75 The objectives of this study were, therefore, to assess the responses of the current
76 earthworm community to past mining activities dating from several centuries ago and for which
77 only scarce data are available in the literature. The impact on the community will be assessed
78 by various community descriptors, as the density and ecological group distribution of
79 earthworms, and originally completed by statistical consideration of bioaccumulation levels of
80 several TMs in earthworm tissues belonging to different morpho-ecological categories.

81

82 **2- Material and methods**

83 **2-1- Study sites**

84 The study site is located in the former mining district of Sainte-Marie-aux-Mines
85 (Vosges Mountains, France). Four forested stations (100 m²), called MA5, CF20, CF28, and
86 CF29, were chosen according to their soil TM concentrations (Table 1) and to the presence of
87 various types of mining wastes: ore dump on CF28, ore-washing sediments on CF29, and
88 tailings from ancient mining wells on CF20. Lastly, according to the low TM concentrations
89 measured in soils, station MA5 constitutes the control station. The habitat descriptors, in terms

90 of dominating tree species and main physicochemical characteristics, are presented in Table 2.
91 More details are also available in Mariet et al. (2016).

92 **2-2- Sampling procedures and earthworm determination**

93 For each station, sampling of autochthonous earthworms was carried out in spring
94 (April) following the mustard method (Singh et al., 2016). Two spreadings (10 L each) of
95 freshly diluted mustard (15 g L^{-1}) were applied, with an interval of 15 minutes, on a triplicate
96 surface of 1 m^2 representative of the entire station. Then, the earthworm sampling was
97 completed by hand sorting up to 30 cm depth (Pelosi et al., 2009). Sampled animals were rinsed
98 and sorted by ecological groups (Bouché, 1977): epigeics, endogeics, epianecics, and anecic
99 strict. The earthworms were left to empty their guts for 48 hours in moistened Petri dishes,
100 individually weighted, pooled by ecological groups, and sacrificed at -80°C . For each station
101 and ecological group, some individuals were stored in 95% alcohol for identification at the
102 species level, when possible, using Bouché's key (1972).

103 Soils were also sampled at each sampling plot at three depths of the soil profile: 0-5 cm,
104 5-15 cm, and 15-30 cm. They were sieved to 2 mm, dried at 30°C , and stored for further TM
105 analyses. According to their ecological niche, ecological groups were associated with particular
106 soil depths: 0-5 cm for epigeic earthworms, 15-30 cm for endogeic earthworms, and 0-30 cm
107 for anecic earthworms.

108 **2-3- Trace metal analyses**

109 The total concentrations of Ag, arsenic (As), cadmium (Cd), cobalt (Co), and Pb in soils
110 (Table 1) were measured on dried samples after hot *aqua regia* digestion ($\text{HNO}_3:\text{HCl}$, 2:5, v/v)
111 by ICP-MS (Thermo X2 Series) at the Chrono-Environment Laboratory. These five metals were
112 chosen according to their significant contents in exploited ores and identified as anomalous
113 elements in soils (Mariet et al., 2016). The analytical precision and accuracy were checked

114 using a standard reference material (SRM) (Sigma Aldrich CRM052 Loamy Clay 1) with
115 recovery rates of 97 ± 4 %, on average for all TMs.

116 Earthworms were freeze-dried, ground, and digested in HNO_3 by hot mineralization
117 before ICP-MS analyses (Thermo X2 Series). Analytical precision and accuracy were checked
118 using SRM (TORT-2, Lobster hepatopancreas; National Standard, Ottawa, ON, Canada). The
119 recovery rates were 100 ± 13 %, on average, for all TMs.

120 **2-4- Soil physicochemical characteristics**

121 Organic matter (OM) content, pH_{water} and texture (sand, silt, and clay) were determined
122 on soils (0-30 cm) by the Laboratoire d'Analyse des Sols at the Institut National de la Recherche
123 Agronomique (INRA) in Arras (France), which has earned COFRAC (French Accreditation
124 Committee) accreditation n°1-1380 for its analytical quality of soil characteristics (Table 2).

125 **2-5- Statistical analyses**

126 The TM concentrations in soils were compared among both the stations and depths using
127 a Kruskal-Wallis test ($p < 0.05$) followed by a post-hoc multiple comparison (pgirmess R
128 package). Difference of distribution of ecological groups between stations has been tested by
129 Chi-square test ($p < 0.05$). Then, differences of total density or density of ecological groups
130 between stations were tested using Tukey HSD ($p < 0.05$). The same procedure was used to
131 highlight significant differences of biomass (Figure S1).

132 Principal component analysis (PCA) was carried out to assess the co-variation between
133 community descriptors (total density and biomass), soil contamination (total Ag, As, Cd, Co,
134 and Pb concentrations) and soil characteristics as texture (sand and silt contents), pH, and OM
135 content.

136 The relationships between TM concentration in earthworms and soil contamination on
137 the one hand and, on the other hand, earthworm density and TM concentration in earthworms
138 were tested separately using nonlinear mixed-effects regression models (nlme R package),
139 integrating the earthworm ecological group as fixed effect and the sampling plot as random
140 intercept. The following models were used:

$$141 \quad [TMs]_{earthworm} = a * \ln([TMs]_{soil}) + b$$

$$142 \quad density = d0 * \exp(-k * [TMs]_{earthworm})$$

143 For all of the models, when residuals were skewed, variance functions (power and
144 exponential) were applied, and the best model was selected according to Akaike's Information
145 Criterion (pgirmess R package). The effect of ecological group was tested using a likelihood-
146 ratio test (LRT, $p < 0.05$). When a significant relationship was found, pairwise Wald t-tests of
147 the estimated coefficients were carried out between ecological groups by re-ordering treatments
148 in nlme models using the *relevel* R function (stats R package).

149 All of the statistics were performed with R (3.4.0) (R Core Team, 2014).

150

151 **3- Results**

152 **3-1- Earthworm community description**

153 The main representative species of each ecological group are summarized in Table 3.
154 The earthworm communities were quite similar between the stations studied with *Lumbricus*
155 sp. in the epigeic group, *Aporrectodea caliginosa* in the endogeic group, *Lumbricus rubellus* in
156 the epianecic group and *Aporrectodea* sp. in the anecic strict group. An endemic species of the
157 Vosges Mountains, *Allolobophora zicsii* (Bouché, 1972), an endogeic, was sampled in the MA5
158 station (Table 3).

159 The total density of earthworms sampled at each station showed significant differences
160 with average values of 57 ± 26 , 41 ± 10 , 9 ± 4 and 10 ± 2 ind m^{-2} for MA5, CF20, CF29, and
161 CF28, respectively (Fig. 1). The density of epigeic earthworms was not significantly different
162 between each station, comprised between 4 and 6 ind m^{-2} . For the other ecological categories,
163 the stations can be grouped into two lots based on significant differences of density: on the one
164 hand, MA5 and CF20, and on the other hand, CF29 and CF28 with lower densities of
165 epianecics, anecic strict, and endogeics (Fig. 1). The same pattern was observed for the biomass
166 of earthworms (Figure S1). The highest average density was reached by the anecic strict in
167 MA5 (45 g m^{-2}) and CF20 (25 g m^{-2}), although their density was the lowest in the stations CF29
168 (0.2 g m^{-2}) and CF28 (0 g m^{-2}).

169 The multivariate analysis allowed linking the community descriptors with the
170 physicochemical characteristics of the stations (Fig. 2). The first axis of the PCA (65% variance
171 explained) exhibited a gradient contrasting the stations according to their contamination by TMs
172 (MA5 and CF20 vs. CF29 and CF28). The density and the biomass of earthworms were
173 negatively correlated to the concentrations of TMs in soils. The second and third axis of the
174 PCA (16% and 13% variance explained, respectively) separated stations according to the soil
175 texture (axis 2) and pH/OM content (axis 3). Among soil characteristics, the texture is
176 correlated, negatively for sand content and positively for clay content, to the density and
177 biomass of earthworms.

178 **3-2- Bioaccumulation of TMs by earthworms**

179 The regressions between TM concentrations in whole earthworm tissues and their levels
180 in soils showed significant dose-response relationships for Ag, As, Co, and Pb, but not for Cd
181 ($p = 0.755$) (Fig. 3A and Table S1). The consideration of the earthworm ecological group did
182 not improve the regression for Cd but allowed to distinguish different responses for the other

183 TMs considered (Fig. 3B). Hence, for Co, only endogeic earthworms showed internal
184 concentrations significantly increasing with soil contamination ($p = 0.014$, Table S1). For Ag,
185 a significant and similar relationship between bioaccumulation and soil concentration was
186 highlighted for the epigeics, the endogeics and the epianecics (Fig. 3B and Table S1), while no
187 significance was found for the anecic strict, with average internal concentrations of 0.91 ± 0.26
188 $\mu\text{g g}^{-1}$. The bioaccumulation of As and Pb by earthworms was important (reaching $103.88 \mu\text{g}_{\text{As}}$
189 g^{-1} and $10,368.06 \mu\text{g}_{\text{Pb}} \text{g}^{-1}$ on CF28) and was significantly related to soil concentration for all
190 ecological groups (Fig. 3B). More precisely, for these two TMs, the epianecics showed the most
191 marked responses, followed by the endogeics, the epigeics, and finally the anecic strict (Table
192 S1).

193 **3-3- Earthworm density response to TM bioaccumulation**

194 Taking into account all the data, significant and negative relationships were found
195 between earthworm density and their internal concentrations of Ag, As, and Pb. It was not the
196 case for Cd ($p = 0.533$) and Co ($p = 0.133$) (Fig. 4 and Table 4). However, considering each
197 ecological group, various response patterns are highlighted. Thus, it appears that the density of
198 epianecics was negatively affected by the soil contamination for the five TMs considered (Table
199 4). Except for Cd ($p = 0.880$), similar results were reported for endogeic earthworms.
200 Conversely, no significant influence of TM accumulation on the density was observed for the
201 epigeic earthworms for all TMs. Finally, only internal concentrations of As and Pb were
202 significantly associated with a decline in the anecic strict density (Table 4).

203

204 **4- Discussion**

205 **4-1- Bioavailability of legacy contamination**

206 The studied sites were characterized by the presence of various mining wastes deposited
207 several centuries ago, which constitute a chronic and diffuse source of TM release to the
208 surrounding soils (Mariet et al., 2014). Physico-chemical analyses also revealed that the type
209 of mining waste drives the contamination levels in soils and the availability of TMs (Ettler,
210 2016; Mariet et al., 2017b). Hence, the sampled earthworms at the four stations showed marked
211 differences in their internal concentrations of numerous TMs, which testifies to their current
212 bioavailability to earthworms as previously demonstrated for other soil-dwelling invertebrates,
213 i.e., snails (Mariet et al., 2016). Interestingly, earthworms (this study) and snails (Mariet et al.,
214 2016) led to similar observations although these two bioindicators were used in different
215 approaches, i.e., passive and active biomonitoring, respectively. The concentrations of TMs in
216 the earthworm tissues of the control station (MA5) were of the same order as those reported
217 from the literature for non-contaminated forest sites (Ma, 2004; Morgan and Morgan, 1990;
218 Spurgeon and Hopkin, 1996). Lead, Ag, As, and Co bioaccumulation in earthworms respond to
219 their concentrations in the soils while Cd does not. This could be explained by the relatively
220 low concentration of this element in soils and its high leachability, especially under acidic
221 conditions (Rékási and Filep, 2015). The largest TM tissue concentrations were observed for
222 Pb ($>10,000 \text{ mg kg}^{-1}$ dry weight at CF28) and were comparable to those measured in heavily
223 contaminated sites (Ernst et al., 2008; Ma, 2004). A study recently showed that despite the age
224 of the mining deposits, ageing attenuation was low for Pb, which was still under bioavailable
225 forms (Mariet et al., 2017b). Arsenic reached more than 100 mg kg^{-1} dry weight in earthworms
226 collected at ore dump station CF28, but these values are lower than those found in the literature,
227 even for mining sites (see for instance, Button et al., 2012), probably in relation to the influence
228 of acidic soil pH on As speciation, mobility, and transfer (Wilson et al., 2010). For Ag and Co,
229 the lack of published data concerning their accumulation in earthworms makes the comparisons
230 with our results difficult. However, the significant concentrations measured in earthworms

231 dwelling in mine waste deposit stations (in average $1.3 \text{ mg}_{\text{Ag}} \text{ kg}^{-1}$ in CF28 and $5.3 \text{ mg}_{\text{Co}} \text{ kg}^{-1}$ in
232 CF29) compared to the control station (MA5) indicate a relatively high exposure to these
233 elements exploited in the valley until the 18th century (Fluck, 2000).

234 Bioaccumulation abilities also depend on the earthworm ecological category. Indeed, in
235 our study, endogeic, and epianecic earthworms showed the highest internal concentrations
236 followed by epigeics and anecic strict. This could be explained by several eco-physiological
237 factors. First, species differences in tissue metal concentration may largely reflect differences
238 in niche separation (Morgan and Morgan, 1999; Qiu et al., 2014). The vertical distribution of
239 different species in the soil profile determines to some extent the exposure of earthworms to
240 contrasted TM bioavailable pools. For instance, epigeic earthworms are less exposed than
241 geophagous species due to their saprophagous feeding behavior on the surface organic horizons
242 of soils and their limited exposure route through dermal surface (Langdon et al., 2003). The
243 results concerning earthworms belonging to the anecic strict category confirm the general
244 tendency toward lower metal contents in tissues of deep-burrowing species (Ernst et al., 2008;
245 Suthar et al., 2008; Tischer, 2009). However, this result was not really expected in our particular
246 context of ancient mining contamination characterized by an increasing contamination with
247 depth. The anecic strict are therefore exposed to elevated total TM concentrations but only low
248 available fractions due to the sequestration of TMs, and especially Pb, in the mineral matrix of
249 ore fragments in soils (Mariet et al., 2017b). The endogeics were the only ecological category
250 to bioaccumulate all five TMs studied significantly. In comparison to the anecic species, which
251 create permanent vertical galleries, the horizontal burrowing system of endogeics may retain
252 more pore water and consequently increase the bioavailability of TMs and transfer through
253 cutaneous uptake (Suthar et al., 2008; Vijver et al., 2003). Lastly, various physiological abilities
254 may also explain the contrasted bioaccumulations observed between earthworms belonging to
255 different ecological categories. Thus, digestive physiology may modulate the assimilation

256 efficiencies of different species (Peijnenburg et al., 2012; Pearce, 1978). Moreover, once
257 assimilated, species-specific biochemical strategies may determine the internal fate of TMs and
258 their subcellular fractionation (detoxification and storage, interaction with sites of toxic action,
259 excretion) (Leveque et al., 2013; Morgan and Morgan, 1992; Morgan and Morgan, 1998; Vijver
260 et al., 2006). The physiological processes involved in the contrasted bioaccumulation patterns
261 need further studies since they may explain the responses of earthworms we observed at the
262 community level.

263

264 **4-2- Community responses to contamination**

265 On the uncontaminated station (MA5), total earthworm density reaches 57 ± 19 ind m⁻²,
266 which is in the range of data reported for European forests (De Wandeler et al., 2016). The
267 distribution within ecological categories is however different with about 7% epigeic, 34%
268 epianecic, 40% anecic strict, and 19% endogeic, reflecting site-specific conditions of the studied
269 area. As an example, we found *Allolobophora zicsii*, an endemic endogeic earthworm species
270 of the Vosges Mountains. A significant decrease of total earthworm density was observed at
271 the stations impacted by mining waste deposits. At the ecological group level, this decline
272 mainly relies on a strong decrease of endogeic and a near-disappearance of anecic and
273 especially anecic strict, which were not retrieved in the CF28 station. More precisely, the results
274 clearly indicate a relationship between the concentrations of TMs accumulated in earthworm
275 tissues and the decline in the density of endogeic and (epi)anecic. Among the TMs studied, Ag,
276 As, and Pb seem particularly involved with internal concentrations exceeding the toxicity
277 thresholds. Indeed, Luo et al. (2014) estimated Pb LC50 (the concentration causing 50 %
278 mortality), EC10, and EC50 (the concentrations causing 10% and 50% effect) values on the
279 survival and reproduction of the earthworm *Eisenia andrei* at 852, 248, and 484 mg_{Pb} kg⁻¹
280 earthworm tissue, respectively. For As, Bustos et al. (2015) determine EC10, 25 and 50 for

281 *Eisenia fetida* response of cocoon production at 38, 47 and 57 mg_{As} kg⁻¹, respectively. Thus,
282 with internal concentrations reaching more than 10,000 and 100 mg kg⁻¹ for Pb and As,
283 respectively, these TMs may have cause fitness disturbances (growth, reproduction) at the
284 individual scale and therefore disruptions of the population structure. Toxicity data for Ag and
285 Co for earthworms are, to our knowledge, not available in the literature.

286 Nevertheless, small populations of earthworms, with particular ecological distribution,
287 are still able to survive even under such heavy exposure to TMs, suggesting potential local
288 adaptation of natural populations. Although no definitive evidence has been clearly
289 demonstrated for earthworms, several recent results suggest that TMs may act as selective
290 pressures in natural populations and that genetic variation exists for genes involved in
291 homeostatic regulation and detoxification of TMs (Anderson et al., 2013; Pauwels et al., 2013;
292 Spurgeon et al., 2011).

293 Finally, beyond the soil contamination, it is well established that other edaphic factors
294 also influence the incidence of earthworms in the environment (De Wandeler et al., 2016). In
295 the present study, the mining operations carried out on the different sites have also disturbed
296 the soil structure and texture. On CF20, the digging of mining wells led to the accumulation of
297 relatively small amounts of excavated materials in comparison to CF28, an ore dump dating
298 back to the 17th century, where tons of tailings (coarse gravel and sand) have been deposited
299 during the mine exploitation. CF29 has been a site of ore washing operations and is
300 characterized by the accumulation of fine and dense particles forming compacted layers (former
301 decantation basins). These specific soil features may likely complicate the activity of
302 earthworms, especially for deep-burrowing species such as anecic strict which have almost
303 completely disappeared at stations CF28 and CF29.

304

305 **5- Conclusion**

306 Although literature is full of ecotoxicological studies regarding the effects of recent
307 industrial contamination on earthworms, there is a lack of data regarding legacy impact related
308 to very ancient mining activities. Here, we demonstrated using a passive biomonitoring
309 campaign that even several centuries after their deposits, TMs from mining wastes are still
310 bioavailable for local earthworm populations. The related TM accumulation in earthworm
311 tissues, along with the disturbance of soil structure, may explain the decline observed in
312 earthworm density and the disturbance of the ecological distribution marked by the decrease of
313 endogeic and anecic species. It also represents significant loads of TMs potentially transferable
314 to the higher trophic levels. From a management point of view, this study finally points out the
315 necessity to consider ancient mining or smelting wastes as still currently hazardous materials
316 which should be included in the framework of ecological risk assessment of polluted soils and
317 sites.

318

319 **Acknowledgements**

320 The authors would like to thank Mickaël Hedde (UMR ECOSYS INRA Versailles) for
321 his help in earthworm identification. We are also grateful to Maxime Mermet, Lorène Roscio,
322 and Coline Beaupuy-Mouret for their help during field work. Financial support was provided
323 by the ADEME, the Région Franche-Comté, the French national program EC2CO-Ecodyn
324 (POLMIN, coord.: F. Gimbert), and the European INTERREG V Oberrhein program “Regio
325 Mineralia” (Coord.: J. Gauthier and P. Fluck, CRESAT, Mulhouse).

326

327 **Supplementary Data:** Figure S1 represents the biomass of earthworms for each ecological
328 group for the four stations. Table S1 gives the model outputs of the relationships between trace
329 metal concentrations in earthworm tissue (mg kg^{-1}) and concentrations in soil.

330

331 **References**

- 332 Anderson, C.J., Kille, P., Lawlor, A.J., Spurgeon, D.J., 2013. Life-history effects of arsenic
333 toxicity in clades of the earthworm *Lumbricus rubellus*. *Environmental Pollution* 172,
334 200–207.
- 335 Bouché, M.B., 1972. Lombriciens de France. *Ecologie et Systématique*. I.N.R.A. (Annales de
336 Zoologie Ecologie Animale N° H.S. 72/2), Paris.
- 337 Bouché, M.B., 1977. Stratégies Lombriciennes. *Bulletin Ecologie Paris* 25, 122–132.
- 338 Bustos, V., Mondaca, P., Verdejo, J., Sauvé, S., Gaete, H., Celis-Diez, J.L., Neaman, A., 2015.
339 Thresholds of arsenic toxicity to *Eisenia fetida* in field-collected agricultural soils
340 exposed to copper mining activities in Chile. *Ecotoxicology and Environmental Safety*
341 122, 448–454.
- 342 Button, M., Koch, I., Reimer, K.J., 2012. Arsenic resistance and cycling in earthworms residing
343 at a former gold mine in Canada. *Environmental Pollution* 169, 74–80.
- 344 De Wandeler, H., Sousa-Silva, R., Ampoorter, E., Bruelheide, H., Carnol, M., Dawud, S.M.,
345 Danila, G., Finer, L., Hättenschwiler, S., Hermy, M., Jaroszewicz, B., Joly, F.-J., Müller,
346 S., Pollastrini, M., Ratcliffe, S., Raulund-Rasmussen, K., Selvi, F., Valladares, F., Van
347 Meerbeek, K., Verheyen, K., Vesterdal, L., Muys, B., 2016. Drivers of earthworm
348 incidence and abundance across European forests. *Soil Biology & Biochemistry* 99,
349 167–178.
- 350 Ernst, G., Zimmermann, S., Christie, P., Frey, B., 2008. Mercury, cadmium and lead
351 concentrations in different ecophysiological groups of earthworms in forest soils.
352 *Environmental Pollution* 156, 1304–1313.
- 353 Ettler, V., 2016. Soil contamination near non-ferrous metal smelters: A review. *Applied*
354 *Geochemistry* 64, 56–74.

355 Fluck, P., 2000. Sainte-Marie-aux-Mines ou Les mines du rêve. Une monographie des mines
356 d'argent. Sultz: Les Editions du Patrimoine Minier.

357 Fluck, P., 2006. Les mines de plomb, cuivre et argent de la Renaissance ont généré des paysages
358 contrastés. L'exemple de l'Alsace et des Vosges (France de l'Est).

359 Langdon, C.J., Pearce, T.G., Meharg, A.A., Semple, K.T., 2003. Interactions between
360 earthworms and arsenic in the soil environment: a review. *Environmental Pollution* 124,
361 361–373.

362 Leveque, T., Capowiez, Y., Schreck, E., Mazzia, C., Auffan, M., Foucault, Y., Austruy, A.,
363 Dumat, C., 2013. Assessing ecotoxicity and uptake of metals and metalloids in relation
364 to two different earthworm species (*Eiseina hortensis* and *Lumbricus terrestris*).
365 *Environmental Pollution* 179, 232–241.

366 Luo, W., Verweij, R.A., van Gestel, C.A.M., 2014. Determining the bioavailability and toxicity
367 of lead contamination to earthworms requires using a combination of physicochemical
368 and biological methods. *Environmental Pollution* 185, 1–9.

369 Ma, W.-C., 2004. Estimating heavy metal accumulation in oligochaete earthworms: a meta-
370 analysis of field data. *Bulletin of Environmental Contamination and Toxicology* 72,
371 663–670.

372 Mariet, A.-L., de Vaufléury, A., Bégeot, C., Walter-Simonnet, A.-V., Gimbert, F., 2016.
373 Palaeo-pollution from mining activities in the Vosges Mountains: 1000 years and still
374 bioavailable. *Environmental Pollution* 214, 575–584.

375 Mariet, A.-L., Gimbert, F., Bégeot, C., Gauthier, J., Fluck, P., Walter-Simonnet, A.V., 2014.
376 Palaeoenvironmental and actual research on contamination by trace metals on the
377 mining district of Sainte-Marie-aux-Mines, Vosges Mountains. In: *Collection Edytem*
378 *Exploitations minières passées et présentes : impacts environnementaux et sociétaux* (in
379 French).

380 Mariet, A.-L., Pauget, B., de Vaufleury, A., Bégeot, C., Walter-Simonnet, A.-V., Gimbert, F.,
381 2017a. Using bioindicators to assess the environmental risk of past mining activities in
382 the Vosges Mountains (France). *Ecological Indicators* 75, 17–26.

383 Mariet, A.-L., Sarret, G., Bégeot, C., Walter-Simonnet, A.-V., Gimbert, F., 2017b. Lead highly
384 available in soils centuries after metallurgical activities. *Journal of Environmental*
385 *Quality*. Special Issue: Synchrotron radiation-based methods for environmental
386 biogeochemistry.

387 Morgan, A.J., Morgan, J.E., 1992. The accumulation and intracellular compartmentation of
388 cadmium, lead, zinc and calcium in two earthworm species (*Dendrobaena rubida* and
389 *Lumbricus rubellus*) living in highly contaminated soil. *Histochemistry* 75, 269–285.

390 Morgan, J.E., Morgan, A.J., 1990. The distribution of cadmium, copper, lead, zinc and calcium
391 in the tissues of the earthworm *Lumbricus rubellus* sampled from one uncontaminated
392 and four polluted soils. *Oecologia* 84, 559–566.

393 Morgan, J.E., Morgan, A.J., 1998. The distribution and intracellular compartmentation of
394 metals in the endogeic earthworm *Aporrectodea caliginosa* sampled from an unpolluted
395 and a metal-contaminated site. *Environmental Pollution* 99, 167–175.

396 Morgan, J.E., Morgan, A.J., 1999. The accumulation of metals (Cd, Cu, Pb, Zn and Ca) by two
397 ecologically contrasting earthworm species (*Lumbricus rubellus* and *Aporrectodea*
398 *caliginosa*): implications for ecotoxicological testing. *Applied Soil Ecology* 13, 9–20.

399 Nahmani, J., Lavelle, P., Lapied, E., van Oort, F., 2003. Effects of heavy metal soil pollution
400 on earthworm communities in the north of France. *Pedobiologia* 47, 663–669.

401 Pauwels, M., Frérot, H., Souleman, D., Vandenbulcke, F., 2013. Using biomarkers in an
402 evolutionary context: Lessons from the analysis of biological responses of oligochaete
403 annelids to metal exposure. *Environmental Pollution* 179, 343–350.

404 Peijnenburg, W., Capri, E., Kula, C., Liess, M., Luttik, R., Montforts, M., Nienstedt, K.,
405 Römbke, J., Sousa, J.P., Jensen, J., 2012. Evaluation of Exposure Metrics for Effect
406 Assessment of Soil Invertebrates. *Critical Reviews in Environmental Science and*
407 *Technology* 42, 1862–1893.

408 Pelosi, C., Bertrand, M., Capoweiz, Y., Boizard, H., Estrade, J. R., 2009. Earthworm collection
409 from agricultural fields: Comparisons of selected expellants in presence/absence of hand
410 sorting. *European Journal of Soil Biology* 45, 176–183.

411 Pérès, G., Vandebulcke, F., Guernion, M., Hedde, M., Beguiristain, T., Douay, F., Houot, S.,
412 Piron, D., Richard, A., Bispo, A., Grand, C., Galsomies, L., Cluzeau, D., 2011.
413 Earthworm indicators as tools for soil monitoring, characterization and risk assessment.
414 An example from the national Bioindicator programme (France). *Pedobiologia* 54S,
415 S77–S87.

416 Pearce, T.P., 1978. Gut contents of some lumbricid earthworms. *Pedobiologia* 18, 153–157.

417 Qiu, H., Peijnenburg, W.J.G.M., van Gestel, C.A.M., Vijver, M.G., 2014. Can commonly
418 measurable traits explain differences in metal accumulation and toxicity in earthworm
419 species? *Ecotoxicology* 23, 21–32.

420 Rékási, M., Filep, T., 2015. Factors determining Cd, Co, Cr, Cu, Ni, Mn, Pb and Zn mobility
421 in uncontaminated arable and forest surface soils in Hungary. *Environmental Earth*
422 *Sciences* 74, 6805–6817.

423 R Core Team, 2014. R: A language and environment for statistical computing. R Foundation
424 for Statistical Computing, Vienna, Austria. URL: <http://www.R-project.org>

425 Singh, J., Singh, S., Vig, A.P., 2016. Extraction of earthworm from soil by different sampling
426 methods: a review. *Environment, Development and Sustainability* 18, 1521–1539.

427 Spurgeon, D.J., Hopkin, S.P., 1996. The effects of metal contamination on earthworm
428 populations around a smelting works – quantifying species effects. *Applied Soil*
429 *Ecology* 4, 147–160.

430 Spurgeon, D.J., Lister, L., Kille, P., Pereira, M.G., Wright, J., Svendsen, C., 2011.
431 Toxicokinetic studies reveal variability in earthworm pollutant handling. *Pedobiologia*
432 54S, S217–S222.

433 Suthar, S., Singh, S., Dhawan, S., 2008. Earthworms as bioindicator of metals (Zn, Fe, Mn, Cu,
434 Pb and Cd) in soils: Is metal bioaccumulation affected by their ecological category?
435 *Ecological Engineering* 32, 99–107.

436 Tischer, S., 2009. Earthworms (Lumbricidae) as bioindicators: the relationship between in-soil
437 and in-tissue heavy metal content. *Polish Journal of Ecology* 57, 513–523.

438 Tondoh, J.E., Monin, L.M., Tiho, S., Csuzdi, C., 2007. Can earthworms be used as bio-
439 indicators of land-use perturbations in semi-deciduous forest? *Biology and Fertility of*
440 *Soils* 43, 585–592.

441 Tylecote, R.F., 1987. The early history of metallurgy in Europe. Longman archaeology series.
442 London. 391 p.

443 Vijver, M.G., van Gestel, C.A.M., van Straalen, N.M., Lanno, R.P., Peijnenburg, W.J.G.M.,
444 2006. Biological significance of metals partitioned to subcellular fractions within
445 earthworms (*Aporrectodea caliginosa*). *Environmental Toxicology and Chemistry* 25,
446 807–814.

447 Vijver, M.G., Vink, J.P.M., Miermans, C.J.H., van Gestel, C.A.M., 2003. Oral sealing using
448 glue: a new method to distinguish between intestinal and dermal uptake of metals in
449 earthworms. *Soil Biology & Biochemistry* 35, 125–132.

450 Wilson, S.C., Lockwood, P.V., Ashley, P.M., Tighe, M., 2010. The chemistry and behaviour
451 of antimony in the soil environment with comparisons to arsenic: a critical review.
452 Environmental Pollution 158, 1169–1181.

453 **Table captions**

454

455 **Table 1:** Concentrations of Ag, As, Cd, Co and Pb ($\mu\text{g g}^{-1}$) for the four stations for three depths
456 (0-5 cm; 5-15 cm; 15-30 cm). Significant differences of concentrations in soils between stations
457 and depths for a TM were highlighted by different letters.

458

459 **Table 2:** Main habitat descriptors of the four stations.

460

461 **Table 3:** Main representative earthworm species sampled in the four stations and for the four
462 ecological groups.

463

464 **Table 4:** Model outputs of the relationships between earthworm density (ind m^{-2}) and their
465 internal concentrations (mg kg^{-1}). Data are given for whole species (total) and each ecological
466 group. SE = Standard Error. For each metal and each model parameter, different letters indicate
467 significant differences.

468

469 **Table 1**

Station	Depth (cm)	Ag	As	Cd	Co	Pb
MA5	0-5	0.34 ± 0.06 ^a	39.97 ± 5.83 ^a	0.35 ± 0.04 ^{ab}	29.14 ± 8.21 ^a	175.69 ± 24.18 ^a
	5-15	0.75 ± 0.04 ^b	57.92 ± 10.53 ^b	0.29 ± 0.05 ^{ab}	25.93 ± 5.81 ^a	357.88 ± 53.64 ^b
	15-30	0.14 ± 0.04 ^c	36.24 ± 6.24 ^a	0.26 ± 0.07 ^{ab}	27.66 ± 4.37 ^a	92.37 ± 11.62 ^c
CF20	0-5	1.10 ± 0.15 ^d	254.89 ± 61.25 ^c	0.41 ± 0.08 ^b	17.74 ± 2.86 ^b	341.63 ± 40.78 ^b
	5-15	0.29 ± 0.05 ^a	150.02 ± 20.13 ^d	0.25 ± 0.04 ^a	18.54 ± 3.13 ^b	177.64 ± 34.72 ^a
	15-30	0.66 ± 0.14 ^b	267.89 ± 56.72 ^c	0.49 ± 0.11 ^b	27.05 ± 6.03 ^a	325.52 ± 87.45 ^b
CF29	0-5	4.69 ± 1.12 ^d	257.85 ± 58.16 ^c	1.10 ± 0.38 ^c	22.99 ± 7.49 ^a	2539.25 ± 374.18 ^d
	5-15	60.41 ± 19.15 ^e	3110.54 ± 514.36 ^d	3.88 ± 0.57 ^d	94.05 ± 23.64 ^c	22,347.63 ± 2795.78 ^e
	15-30	132.23 ± 36.72 ^f	3574.07 ± 427.10 ^d	8.21 ± 0.95 ^e	91.43 ± 8.67 ^c	54,048.87 ± 5708.36 ^f
CF28	0-5	14.80 ± 1.40 ^g	888.25 ± 43.67 ^e	1.33 ± 0.10 ^c	18.12 ± 1.61 ^{ab}	8582.87 ± 385.3 ^g
	5-15	30.50 ± 1.78 ^h	1658.30 ± 109.92 ^f	2.08 ± 0.18 ^f	29.10 ± 3.46 ^a	12,153.67 ± 849.09 ^g
	15-30	65.79 ± 6.12 ^e	2334.15 ± 145.11 ^g	3.54 ± 2.13 ^{cdf}	48.72 ± 2.13 ^d	24,748.40 ± 3209 ^e

470

471

472 **Table 2**

Station	Altitude (m a.s.l.)	Dominating tree species	pH water	Clay (g kg ⁻¹)	Silt (g kg ⁻¹)	Sand (g kg ⁻¹)	C _{org} (g kg ⁻¹)	CEC (cmol ⁺ kg ⁻¹)
MA5	730	<i>Abies alba</i> , <i>Acer pseudoplatanus</i> , <i>Fagus sylvatica</i>	4.6 ± 0.1	266 ± 31	286 ± 29	448 ± 59	75.5 ± 7.6	25.7 ± 0.6
CF29	782	<i>Abies alba</i> , <i>Acer pseudoplatanus</i>	5.0 ± 0.1	99 ± 34	305 ± 139	595 ± 172	19.2 ± 1.6	8.6 ± 1.2
CF28	804	<i>Abies alba</i> , <i>Picea abies</i>	4.3 ± 0.1	133 ± 13	242 ± 20	625 ± 33	52.3 ± 17.5	15.5 ± 3.4
CF20	856	<i>Abies alba</i> , <i>Fagus sylvatica</i>	4.7 ± 0.05	131 ± 8	234 ± 21	635 ± 28	27.4 ± 5.1	11.9 ± 1.6

473

474 **Table 3**

Station	Epigeic	Endogeic	Epianecic	Anecic strict
MA5	<i>Lumbricus moliboeus</i>	<i>Allolobophora zicsii</i> <i>Aporrectodea caliginosa</i>	<i>Lumbricus rubellus</i> <i>rubellus</i> <i>Lumbricus rubellus</i> <i>friendoides</i>	<i>Aporrectodea</i> sp.
CF20	<i>Allolobophora antipai</i> (<i>vogesiana?</i>)	<i>Aporrectodea caliginosa</i> <i>Aporrectodea longa</i>	<i>Lumbricus rubellus</i> <i>rubellus</i>	<i>Aporrectodea</i> (<i>nocturna?</i>)
CF28	<i>Lumbricus</i> sp.	<i>Aporrectodea caliginosa</i>	<i>Lumbricus rubellus</i> <i>rubellus</i>	-
CF29	<i>Lumbricus</i> sp.	<i>Allolobophora rosea</i> <i>vedovinii</i> <i>Aporrectodea caliginosa</i>	<i>Lumbricus rubellus</i> <i>rubellus</i>	<i>Aporrectodea</i> sp.

475

Metal	Constant	Total			Epigeic			Epianeic			Anecic strict			Endogeic		
		value	SE	<i>p</i> -value	value	SE	<i>p</i> -value	value	SE	<i>p</i> -value	value	SE	<i>p</i> -value	value	SE	<i>p</i> -value
Ag	d0	1.251	0.108	<0.001	0.723 ^a	0.211	0.001	1.517 ^b	0.182	<0.001	1.797 ^{ab}	0.639	0.007	1.183 ^{ab}	0.156	<0.001
	-k	-1.721	0.542	0.002	-0.029 ^a	1.197	0.981	-3.075 ^b	0.734	<0.001	-1.768 ^{ab}	1.306	0.182	-1.890 ^{ab}	0.695	0.009
As	d0	1.518	0.173	<0.001	0.697 ^a	0.194	<0.001	2.125 ^b	0.359	<0.001	1.999 ^b	0.428	<0.001	1.565 ^b	0.326	<0.001
	-k	-0.444	0.105	<0.001	0.022 ^a	0.189	0.906	-0.733 ^b	0.157	<0.001	-0.478 ^b	0.179	0.010	-0.557 ^b	0.195	0.006
Cd	d0	1.031	0.278	<0.001	0.529 ^a	0.306	0.090	3.855 ^a	1.837	0.041	0.212 ^a	0.209	0.316	0.755 ^a	0.432	0.087
	-k	-0.184	0.293	0.533	0.331 ^a	0.603	0.586	-2.041 ^b	0.694	0.005	1.581 ^{ac}	0.921	0.093	0.076 ^{abc}	0.506	0.880
Co	d0	1.348	0.373	<0.001	0.637 ^{ab}	0.340	0.067	11.03 ^{ab}	7.205	0.132	0.172 ^a	0.143	0.233	1.872 ^b	0.620	0.004
	-k	-0.644	0.421	0.133	0.175 ^{ac}	0.761	0.819	-4.090 ^b	1.104	<0.001	2.488 ^a	1.078	0.025	-1.213 ^c	0.509	0.022
Pb	d0	2.129	0.359	<0.001	0.805 ^a	0.273	0.005	2.151 ^b	0.352	<0.001	24.75 ^{ab}	22.78	0.283	2.843 ^b	0.898	0.003
	-k	-0.332	0.057	<0.001	-0.039 ^a	0.115	0.734	-0.403 ^b	0.083	<0.001	-1.152 ^c	0.351	0.002	-0.443 ^{bc}	0.122	<0.001

478 **Figure captions**

479

480 **Figure 1:** Distribution of individuals in ecological groups, expressed as density (mean \pm S.D.,
481 individuals m^{-2}). Significant differences of density between stations for an ecological group
482 were highlighted by different letters.

483

484 **Figure 2:** Principal component analysis between earthworm community descriptors (total
485 density and biomass), soil contamination (total Ag, As, Cd, Co, and Pb concentrations) and soil
486 characteristics as texture (sand and silt contents), pH, and OM content. Left: Axis 1 and 2;
487 Right: Axis 1 and 3. Stations (MA5, CF20, CF28 and CF29) are also projected.

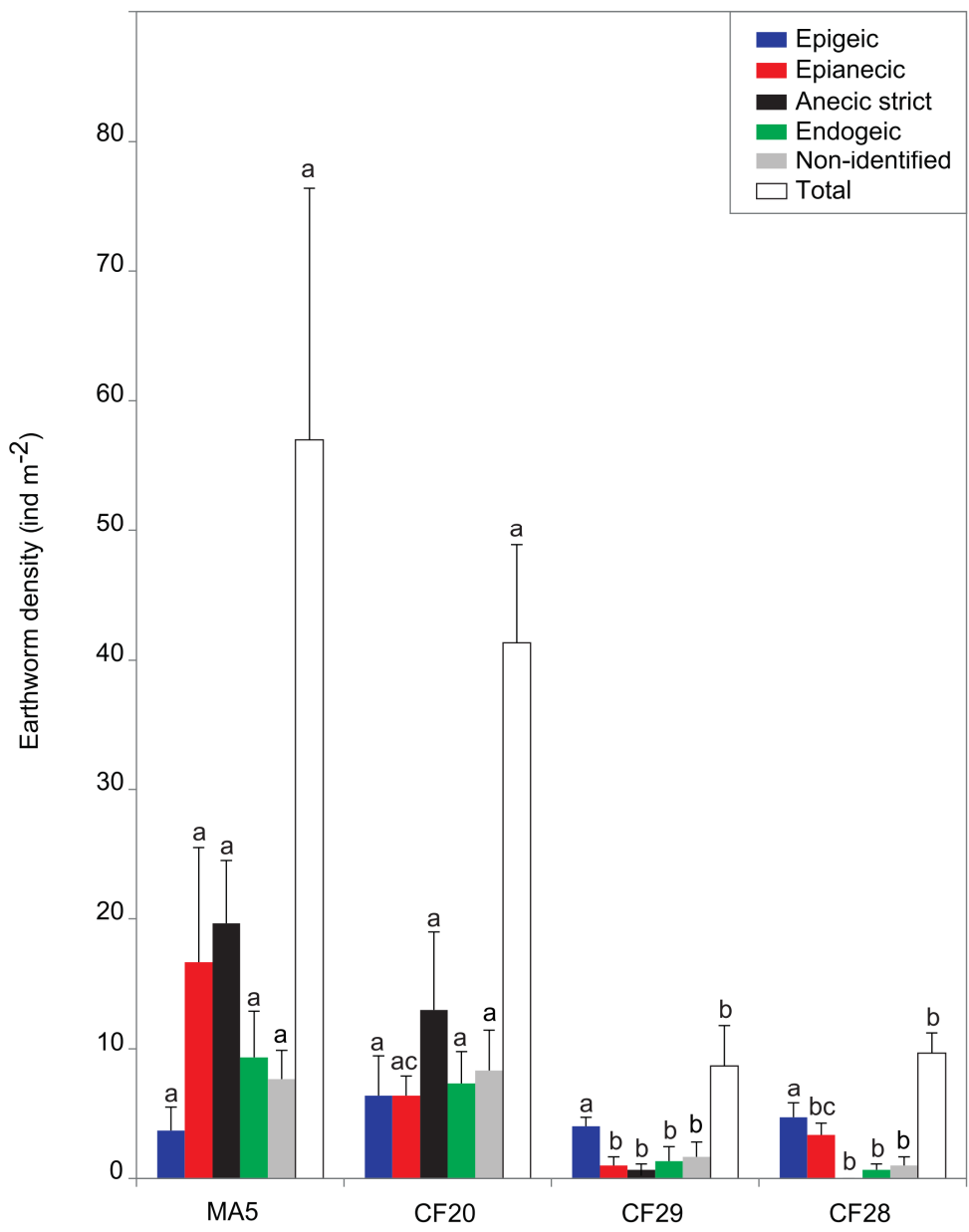
488

489 **Figure 3:** Modelled relationships between trace metal concentrations in earthworm tissues (mg
490 kg^{-1}) and concentrations in soil (mg kg^{-1}). (A): Model fitted to the whole data. (B): Models fitted
491 to each ecological group. Details about model outputs for each ecological group are given in
492 Table S2.

493

494 **Figure 4:** Modelled relationships between earthworm density (ind m^{-2}) and trace metal
495 concentrations in their tissues (mg kg^{-1}). The model was fitted to the whole data. Details about
496 model outputs for each ecological group are given in Table 4.

497

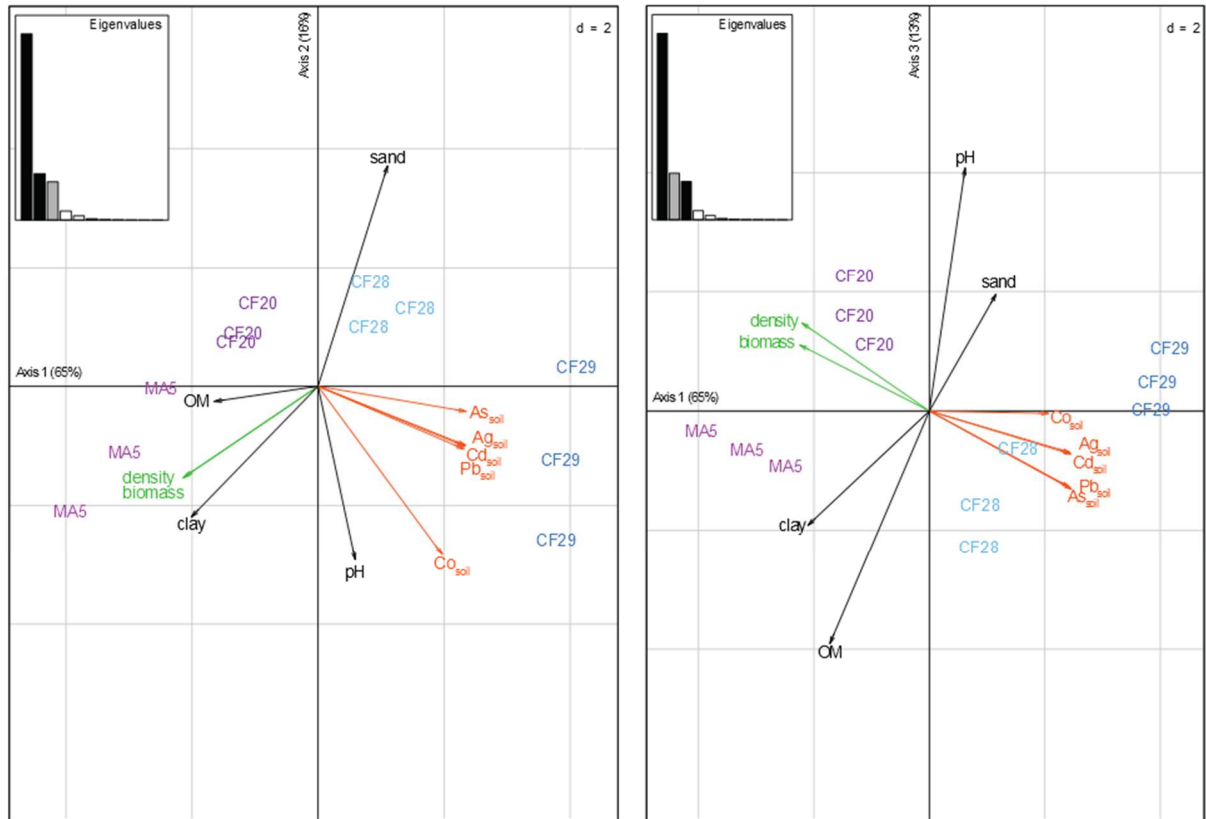


499

500

501 **Figure 2**

502



503

504

505 **Figure 3**

506

507

508

509

510

511

512

513

514

515

516

517

518

519

520

521

522

523

524

525

526

527

528

529

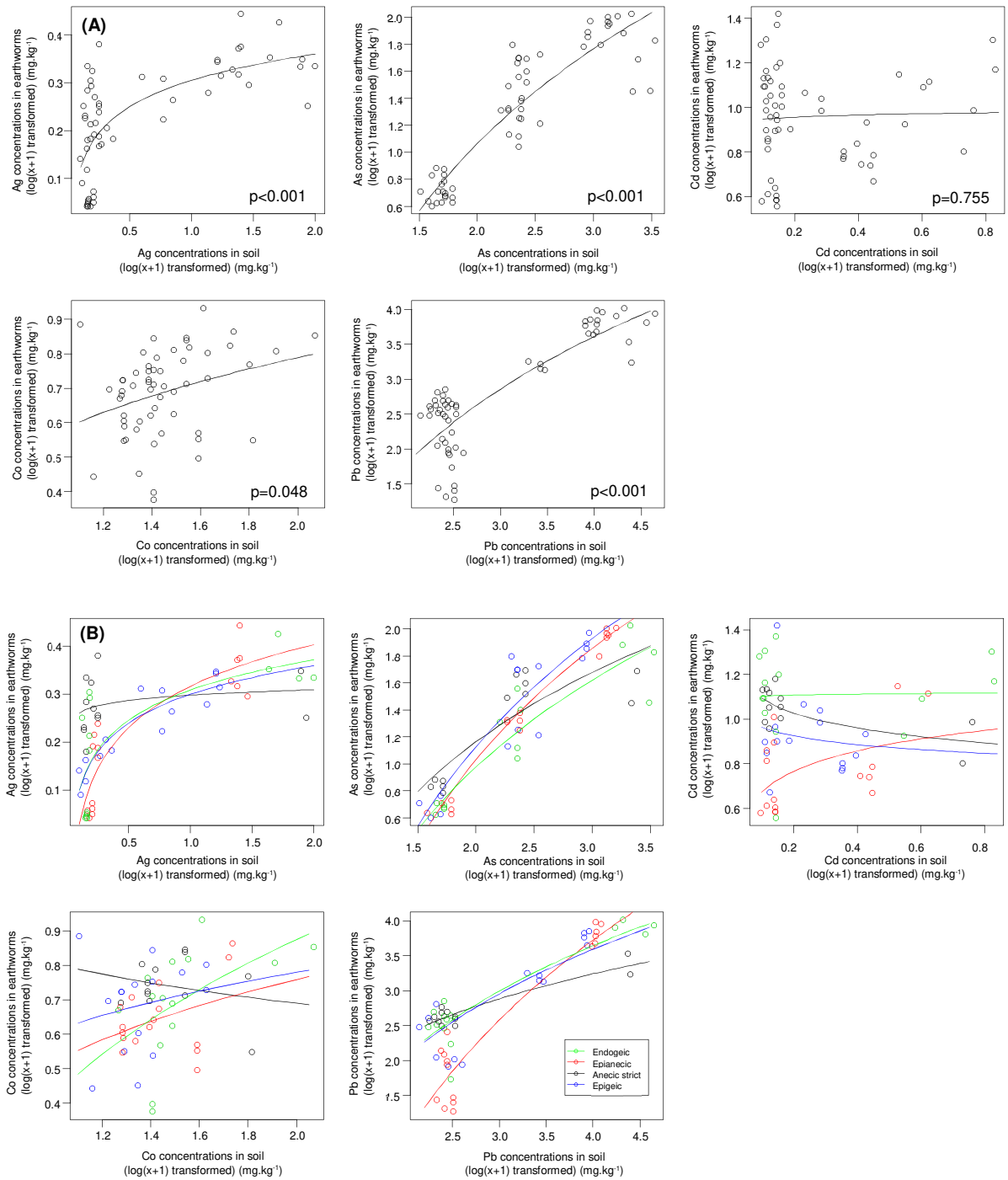
530

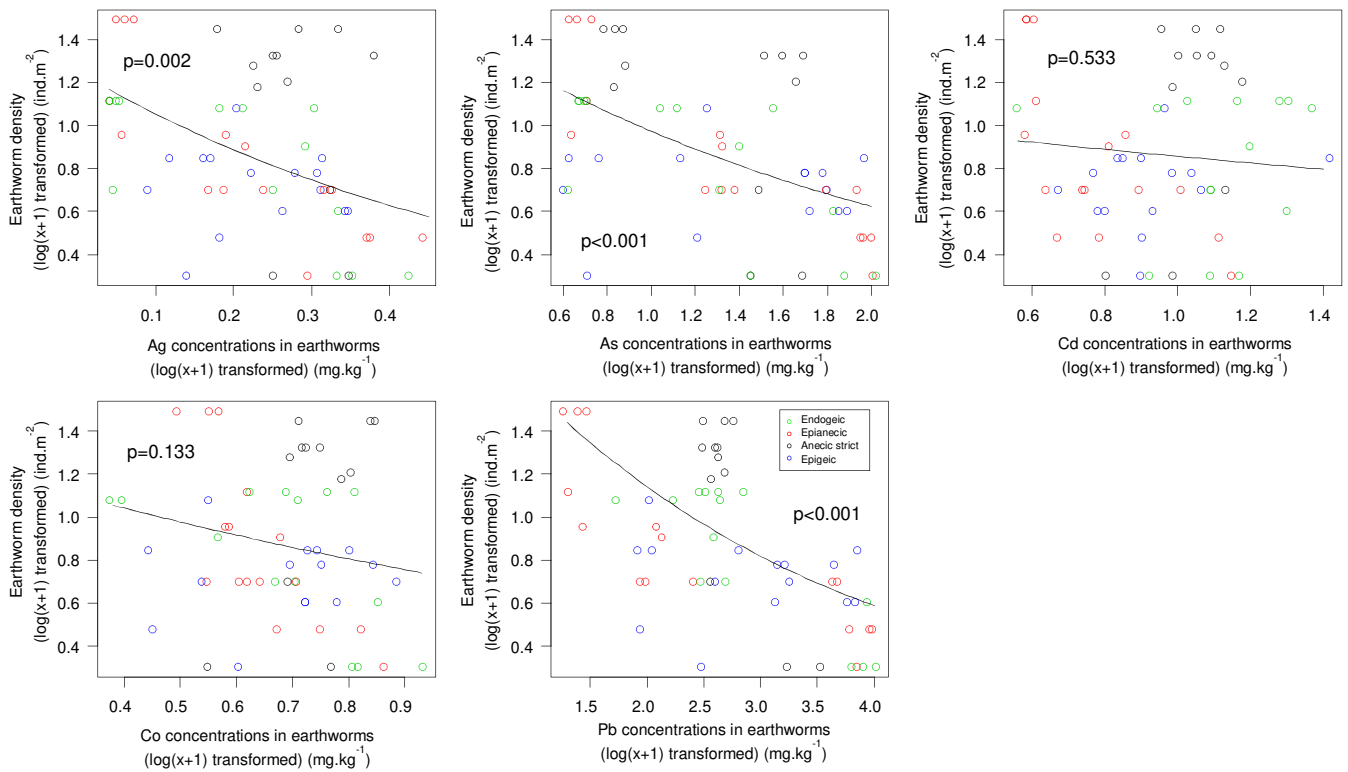
531

532

533

534





1 **Generated compounds at the V-slag/CaO diffusion surface and diffusion characteristics of V**
2 **and Ca in calcium vanadate**

3 Declarations of interest: none

4 Hong-Rui Yue ¹⁾, Xiang-Xin Xue ¹⁾*

5 1) School of Metallurgy, Northeastern University, Shenyang 110819, China

6 Corresponding author: Xiang-Xin Xue; e-mail: xuexx@mail.neu.edu.cn;

7 **Email:** Hong-Rui Yue, hongrui.neu@gmail.com;

8 Xiang-Xin Xue, xuexx@mail.neu.edu.cn;

9

10

11

12

13

14

15

16

17

18

19

20

21

22

23

24

25

26

27

28

29

30

31

32

33

34

35

36

37

Abstract

Vanadium slag/CaO diffusion couples were prepared to study the diffusion characteristics of the vanadium slag/CaO interface at 1083 K in the air. The generated phases at different regions were characterized by EPMA, EDS, XRD, and element maps analysis. At the vanadium slag surface that the diffused Ca dose not reached, the main generated phases were Mn_2O_3 and Fe_2O_3 . V^{3+} was oxidized to V^{5+} and reacted with the Ca^{2+} to form a small amount of $Ca_2V_2O_7$. Cr was at a disadvantage compared with V in occupying the original Ca^{2+} of the slag. At the vanadium slag surface that the diffused Ca had reached, the main generated phases were $Ca_2V_2O_7$. At the CaO surface, the main generated phases were $Ca_2V_2O_7$ and $Ca_3V_2O_8$. The interdiffusion coefficients were calculated by a new approach that modified from the Boltzmann-Matano method including the determination of the Matano surface, calculation of the integral and differential using the raw data of the concentration profiles. As the molar fraction of Ca was in the range of 0.15 to 0.86, the average interdiffusion coefficient of Ca^{2+} was $2.54 \times 10^{-8} \text{ cm}^2 \cdot \text{s}^{-1}$. The average interdiffusion coefficient of V^{5+} at the V molar fraction of 0.001 to 0.43 was $1.96 \times 10^{-8} \text{ cm}^2 \cdot \text{s}^{-1}$.

keywords: Vanadium slag, calcium roasting, diffusion couple, diffusion coefficient, Boltzmann-Matano method

1. Introduction

Vanadium slag (V-slag) usually refers to the solid slag produced in the converter during smelting the vanadium titanium magnetite. As a byproduct of iron making, V-slag contains a large amount of low-valent V which is often extracted by the process of crushing, iron removal, roasting, leaching, precipitation and calcining, etc. Among these processes, roasting is the first one that

61 mainly involves chemical reactions, which makes it more complicated and essential. The primary
62 purpose of roasting is to oxidize the low-valent V in the V spinels into high-valent V and enrich it
63 in the vanadates that can be leached out. At first, sodium salts were proposed as the additives in
64 roasting V-slag, NaCO_3 [1,2], mixture of NaOH and NaNO_3 [3], or NaOH [4] react with V-slag to
65 generate water-soluble soluble vanadates which can be leached in aqueous solution. Under the
66 optimal conditions, almost 100% V can be recovered from the V-slag [4]. In recent years, the sodium
67 salts were gradually abandoned in the roasting due to the severe groundwater pollution caused by
68 sodium ions [5], and calcium salts were proposed as the roasting additives.

69 Zhang [6] studied the process of roasting V-slag powders with CaO powders by
70 thermogravimetric analysis, and the results showed that the V spinels were oxidized and
71 decomposed as the temperature increasing. When the temperature reached 930 K, the oxidized V
72 begun to react with CaO and form calcium vanadates. Cao [7] and Zhang [8] studied the effect of
73 experimental parameters on the V recovery from roasting V-slag powders with CaO powders. The
74 optimal roasting temperature, roasting time, and mass ratio of CaO to V_2O_5 can be inferred as 1123
75 K, 1.5-2.5 hours, and 0.5-0.7, respectively. The reports about roasting V-slag with CaO are
76 relatively rare, and the research method is limited to simulate the roasting system by mixing the V-
77 slag powders and CaO powders. The species of the generated phases are still controversial, much
78 less the distribution of them around the reaction interface. Therefore, more systematic studies of
79 roasting V-slag with CaO are necessary to carry out, and the research methods that can intuitively
80 reflect the interfacial reaction characteristics should be introduced.

81 Preparing the diffusion couple is an intuitive way to study the properties of the reaction
82 interface by coupling dissimilar materials [9]. Simulating reaction systems can help in understanding

83 the phase transformations and the growth of intermediate phases by diffusion-controlled processes
84 [10]. Usually, two materials of different compositions are joined at a sharp planar interface and
85 subjected to heat treatment at a fixed elevated temperature [11]. In the present work, the V-slag/CaO
86 diffusion couples were prepared and roasted at 1083 K which summarized from the optimal roasting
87 parameters [6-8]. In addition to characterizing the diffusion interface of the V-slag/CaO diffusion
88 couple, a new method was proposed to determine the Matano surface and calculate the interdiffusion
89 coefficients. The concentration profiles obtained by EPMA can be directly applied to the new
90 method.

91

92 **2. Experimental**

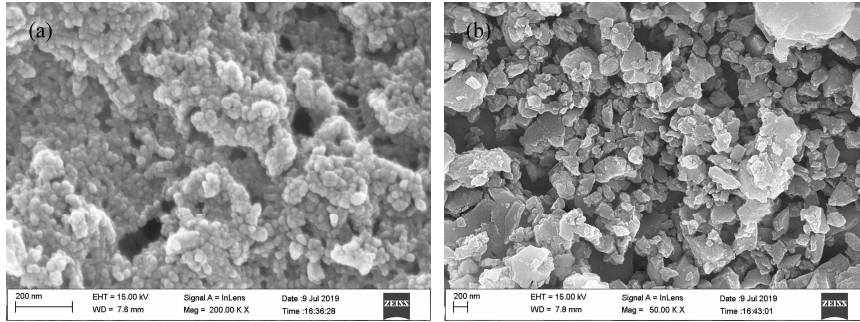
93

94 **2.1. Materials**

95

96 Analytical reagent grade CaO was supplied by Sinopharm Chemical Reagent Co., Ltd. V-slag
97 was gathered from HBIS Group ChengSteel Company, and the composition was analyzed by X-ray
98 fluorescence (XRF, ZSX100e, Rigaku, Japan) and listed in Table 1. The CaO powders and V-slag
99 powders were ball-milled by the high energy ball Vario-Planetary Mill (Pulveristte 4, Fritsch,
100 German) for 3 hours. The diameters of CaO powders and V-slag powders were evaluated by field
101 emission scanning electron microscopy (SEM, Ultra Plus, Carl Zeiss GmbH, Jena, Germany) and
102 shown in Fig. 1(a) and Fig. 1(b), respectively. The particle size of CaO and V-slag are distributed
103 around 20 nm and 200 nm, respectively.

104



105

106

Fig. 1. SEM photographs of CaO particles (a) and raw V-slag particles (b) milled for 3 hours. The

107

ratio of ball to powder was 10:1; the speed of the main-plane and vice-plane were 300 and 150 r/min,

108

respectively; the diameter of the zirconia ball was 10 mm.

109

110

Table 1

111

Chemical composition of the V-slag analyzed by XRF (mass fraction, %)

Fe ₂ O ₃	SiO ₂	MnO ₂	TiO ₂	V ₂ O ₅	MgO	Al ₂ O ₃	CaO	Cr ₂ O ₃
43.4993	14.6256	10.8470	10.2746	8.3874	3.0010	2.6832	2.5803	2.4125

112

113

2.2. Preparation of V-slag/CaO diffusion couple

114

115

Fig. 2 presents the schematic diagram of preparing the V-slag/CaO diffusion couple. As shown

116

in Fig. 2(a) through Fig. 2(d), the CaO powders were pressed (14130 N) into a pellet of 30 mm

117

diameter and 5 mm thickness in the stainless-steel die. As shown in Fig 2(e) through Fig. 2(h),

118

according to the method [12] that can obtain the dense CaO pellet, here, the CaO pellet was hot-

119

pressed in the graphite die at 1573 K for 120 minutes in the vacuum hot-pressing furnace with the

120

vacuum of 20 Pa. The two circular surfaces of the sintered CaO pellet in Fig. 2(h) were polished

121

using SiC sandpapers (23 μm, 13 μm, and 6.5 μm) with diamond polishing paste (1 μm). As shown

122

in Fig. 2(i) through Fig. 2(l), similar to the embedding method of preparing a diffusion couple [13],

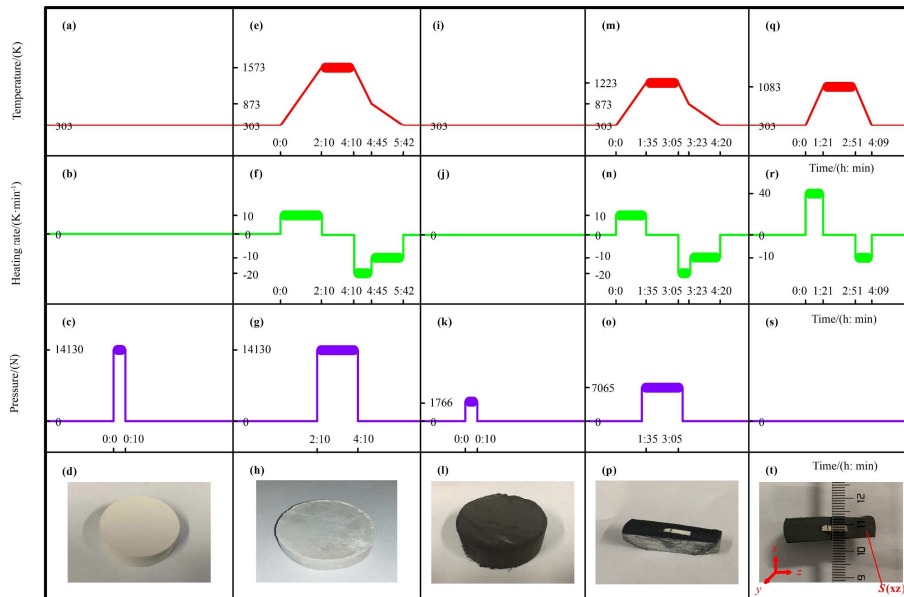
123

here, a quarter of the CaO pellet was embedded into the V-slag powders and pressed (1766 N) into

124

a pellet of 30 mm diameter and 10 mm thickness in a stainless-steel die. As shown in Fig. 2(m)

125 through Fig. 2(p), the V-slag pellet with the CaO pellet were hot-pressed (7065 N) in the graphite
 126 die at 1223 K for 90 minutes in the vacuum hot-pressing furnace with the vacuum of 20 Pa. The
 127 V-slag/CaO pellet was cut into two pieces, and the diffusion surface was polished using sandpapers
 128 and diamond polishing paste. As shown in Fig. 2(q) through Fig. 2(t), the V-slag/CaO diffusion
 129 couple was heated to 1083 K and maintained at this temperature for different time in the muffle
 130 furnace. The surface directly contacted with the air during the roasting was named $S(xz)$. Besides,
 131 the graphite die was coated with boron nitride to prevent carbon contamination.
 132



133
 134 **Fig. 2.** Schematic diagram of preparing the V-slag/CaO diffusion couple.

135
 136 **2.3. Calculation of interdiffusion coefficients**

137
 138 Fick's second law was proposed to describe the diffusion flux by the concentration gradient
 139 and diffusion coefficient [14]. Matano [15] transformed the partial differential equation of Fick's
 140 second law [16] to ordinary differential equation utilizing the Boltzmann parameter [17], and

141 suggested using Eq. (1) to determine the variation of the diffusion coefficient with concentration.

142 Eq. (1) which known as the Boltzmann-Matano formula was widely used to calculate the

143 interdiffusion coefficient of the diffusion couple with the initial conditions in Eq. (2) [18]. The

144 integral and differential in Eq. (1) can be graphically expressed by the area (A_{abgf}) and the slope (k)

145 in Fig. 3(a), respectively. Then, the interdiffusion coefficient at a certain concentration (C') can be

146 expressed as Eq. (3). The key to the Boltzmann-Matano method is to find a particular location that

147 satisfies Eq. (4), and this location was named Matano surface [19]. Eq. (4) can be graphically

148 explained as that the area enclosed by C_a , C and the Matano surface equals to that enclosed by C_e ,

149 C and the Matano surface. Namely, the critical step is to find the point m on the concentration

150 profiles that makes A_{abm} equals to A_{dem} . However, the concentration profiles of the multiphase

151 materials, such as the V concentration profiles on the V-slag surface in the present work, are always

152 too fluctuant to calculate the integral and differential in Eq. (1). Inspired by the works of Appel [20]

153 and Wagner [21], this paper makes the following modifications to the Boltzmann-Matano method.

154 Firstly, the integral variable in Eq. (4) is changed from dC to dx , and Eq. (4) is expressed as Eq. (5).

155 At the same time, the Riemann integral suggests that the area of a definite integral can be represented

156 by the sum of the areas of the little rectangles. Thus, as shown in Fig. 3(b), the areas defined by C_a ,

157 C and the Matano surface (A_{afh}) and C_e , C and the Matano surface (A_{efj}) can be expressed as Eq. (6)

158 and Eq. (7), respectively. As shown in Fig. 3(c), when A_{afh} equals to A_{efj} , the Matano surface (point

159 m) is determined. Secondly, the Matano surface is set as the origin ($X=0$) of a new X -axis. As shown

160 in Fig. 3(d), A_{abgf} can be expressed as the sum of A_{afh} and A_{hbfg} and calculated as Eq. (8). Thirdly,

161 the slopes are determined numerically using the five-point differentiation formulae [22] as given in

162 Eq. (9) and Eq. (10). Finally, the interdiffusion coefficient can be calculated by Eq. (11). The more

163 information about the new method of calculating the interdiffusion coefficient can be seen in our
 164 patent [23].
 165

$$166 \quad D = -\frac{1}{2t} \frac{\int_{C_a}^{C'} x dC}{\left(\frac{dC}{dx}\right)_{C=C'}} \quad (1)$$

$$167 \quad C(x, 0) = \begin{cases} C_a, & x < 0 \\ C_e, & x > 0 \end{cases} \quad (2)$$

$$168 \quad D = -\frac{1}{2t} \frac{A_{abgf}}{k} \quad (3)$$

$$169 \quad \int_{C_a}^{C_m} x dC = -\int_{C_m}^{C_e} x dC \quad (4)$$

$$170 \quad \int_{x_a}^{x_m} C dx = -\int_{x_m}^{x_e} C dx \quad (5)$$

$$171 \quad A_{afh} = \sum_{i=a}^{i=f} (C_a - C_i) \Delta x \quad (6)$$

$$172 \quad A_{efj} = \sum_{i=f}^{i=e} (C_i - C_e) \Delta x \quad (7)$$

$$173 \quad A_{abgf} = \begin{cases} \sum_{i=a}^{i=f} (C_a - C_i) \Delta X + (C_a - C')(0 - X_{C'}), & X < 0 \\ \sum_{i=f}^{i=e} (C_i - C_e) \Delta X + (C' - C_e)(X_{C'} - 0), & X > 0 \end{cases} \quad (8)$$

174 For interior points:

$$175 \quad k = \frac{1}{12\Delta X} (C_{X'-2\Delta X} - 8C_{X'-\Delta X} + 8C_{X'+\Delta X} - C_{X'+2\Delta X}) \quad (9)$$

176 For end-points:

$$177 \quad k = \frac{1}{12\Delta X} (-25C_{X'} + 48C_{X'+\Delta X} - 36C_{X'+2\Delta X} + 16C_{X'+3\Delta X} - 3C_{X'+4\Delta X}) \quad (10)$$

$$178 \quad D = \begin{cases} -\frac{1}{2t} \frac{\sum_{i=a}^{i=f} (C_a - C_i) \Delta X + (C_a - C')(0 - X_{C'})}{\frac{1}{12\Delta X} (C_{X'-2\Delta X} - 8C_{X'-\Delta X} + 8C_{X'+\Delta X} - C_{X'+2\Delta X})}, & X < 0, \text{interior points} \\ -\frac{1}{2t} \frac{\sum_{i=f}^{i=e} (C_i - C_e) \Delta X + (C' - C_e)(X_{C'} - 0)}{\frac{1}{12\Delta X} (C_{X'-2\Delta X} - 8C_{X'-\Delta X} + 8C_{X'+\Delta X} - C_{X'+2\Delta X})}, & X > 0, \text{interior points} \\ -\frac{1}{2t} \frac{\sum_{i=a}^{i=f} (C_a - C_i) \Delta X + (C_a - C')(0 - X_{C'})}{\frac{1}{12\Delta X} (-25C_{X'} + 48C_{X'+\Delta X} - 36C_{X'+2\Delta X} + 16C_{X'+3\Delta X} - 3C_{X'+4\Delta X})}, & X < 0, \text{end-points} \\ -\frac{1}{2t} \frac{\sum_{i=f}^{i=e} (C_i - C_e) \Delta X + (C' - C_e)(X_{C'} - 0)}{\frac{1}{12\Delta X} (-25C_{X'} + 48C_{X'+\Delta X} - 36C_{X'+2\Delta X} + 16C_{X'+3\Delta X} - 3C_{X'+4\Delta X})}, & X > 0, \text{end-points} \end{cases} \quad (11)$$

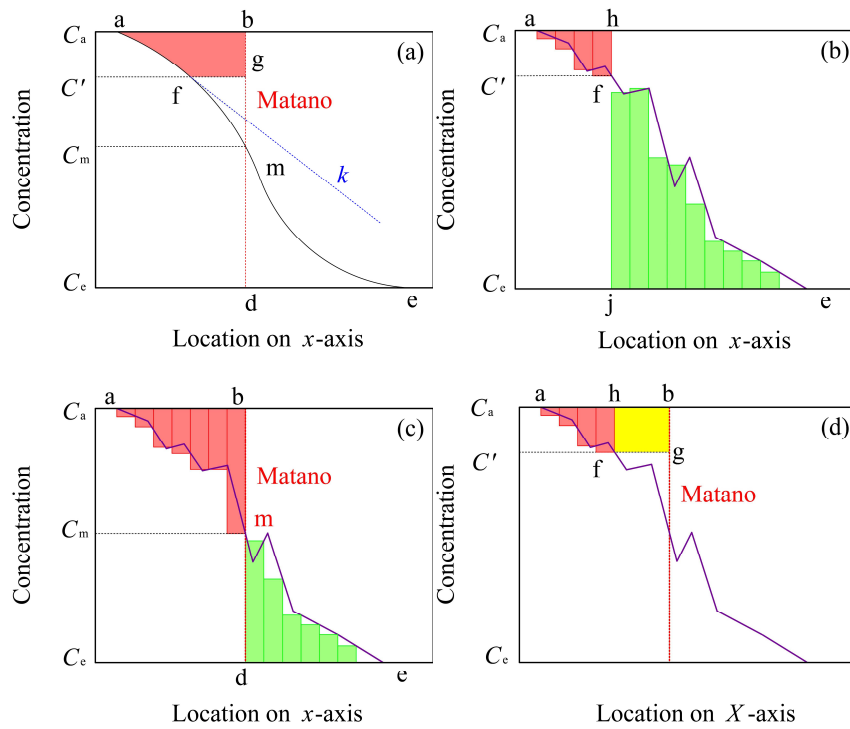
179

180 Where D is the interdiffusion coefficient ($\text{cm}^2 \cdot \text{s}^{-1}$). C is the concentration (g or mol). t is the time

181 (s). x is the location on the x -axis (μm). A is the area (μm^2). k is the slope. X is the location on the

182 X-axis (μm).

183



184

185

186 **Fig. 3.** Graphical interpretation of calculating the interdiffusion coefficient based on the Boltzmann-

187 Matano method.

188

189 2.4. Characterization

190

191 The diffusion surface sprayed of C was analyzed by the electron probe microanalysis (EPMA,

192 JXA-8530F, JEOL, Japan) with the accelerating voltage of 15 kV. The crystalline phases at different

193 locations on the diffusion surface were identified by the X-Ray diffraction (XRD, SmartLab, Rigaku,

194 Japan) with Cu $K\alpha$ radiation ($\lambda=1.54056\text{\AA}$), scanning area of $0.5\text{ mm} \times 0.5\text{ mm}$, and scanning rate

195 of $5^\circ/\text{min}$.

196

197 3. Results

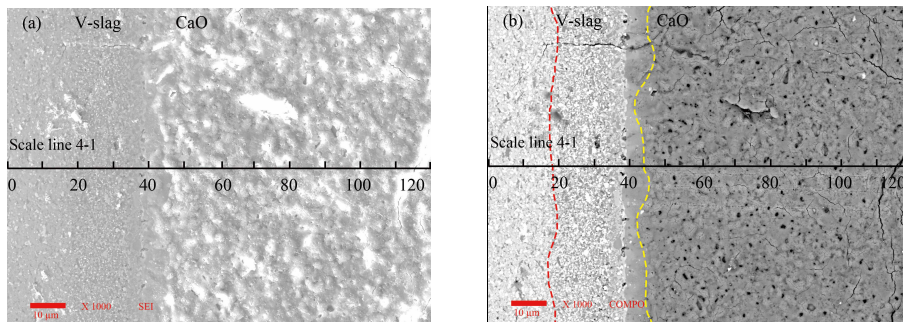
198

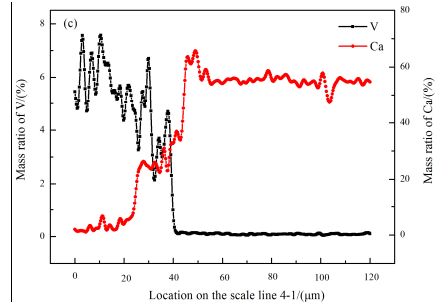
199 **3.1. The thickness of the transport layer at $S(xz)$ before roasting in the air**

200

201 The cross-sectional views of the diffusion interface before roasting in the air are shown in Fig.
202 4(a) and 4(b). The red dashed curve and the yellow dashed curve represent the ending diffusion
203 boundary of Ca on the V-slag surface and the ending diffusion boundary of V on the CaO surface,
204 respectively. A narrow transport layer (L_0), 25.5 μm approximately, is presented at the diffusion
205 surface, which means the degree of the reaction between the low-valent V and CaO is very slight.
206 Detecting of concentration by EPMA is performed along the scale line 4-1 in Fig. 4(a) and Fig. 4(b),
207 and the raw data are plotted in Fig. 4(c). From 15 μm to 40 μm , the V profiles show a general
208 downward trend; the Ca profiles present a general upward trend. While, the fluctuating data can also
209 be seen both on the V profiles and Ca profiles, especially that on the V-slag surface. As given in
210 Table 1, the V-slag already contains a small amount of Ca before roasting, and the generated phases
211 after roasting are very complicated. Therefore, it is challenging to precisely determine the ending
212 diffusion boundary of Ca on the V-slag surface by the following SEI-SEM photographs, COMPO-
213 SEM photographs or the concentration profiles.

214





215

216 **Fig. 4.** Cross-sectional views and concentration profiles of the V-slag/CaO interface annealed at
 217 1223 K for 1.5 hours with the vacuum of 20 Pa.

218

219 **3.2. The diffusion of V and Ca at S(xz) roasted in the air with different time**

220

221 The cross-sectional views of the diffusion interface after roasting in the air for different time

222 and the corresponding concentration profiles are shown in Fig. 5. As illustrated in Fig. 5, the

223 diffusion thickness (L_x) increases with the increase of the roasting time. The diffusion thickness is

224 evaluated by the graphical method [24], and it shows a linear relationship with the square root of

225 roasting time as illustrated in Fig. 6. As usual, three theories were proposed to explain the migration

226 during the diffusion process: the interstitial mechanism [25], the substitutional mechanism [26], and

227 the vacancy mechanism that was widely accepted in metallurgy [27-29]. The vacancy mechanism

228 is that a rise in temperature increases the diffusive mobility of cations; some of them overcome the

229 potential barrier (binding energy in the crystal lattice) and jump [30,31]. The jumped cations diffuse

230 in counter directions toward each other through the cation vacancies and maintain the electrical

231 neutrality at the diffusion interface. The reactions between V_2O_5 and CaO in roasting V-slag were

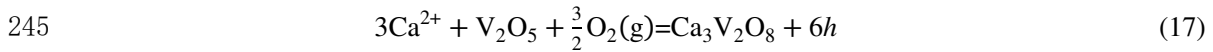
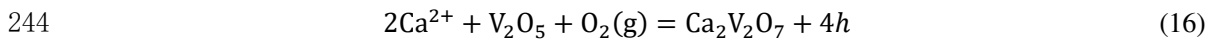
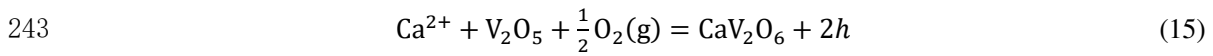
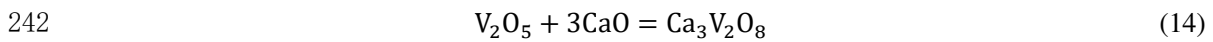
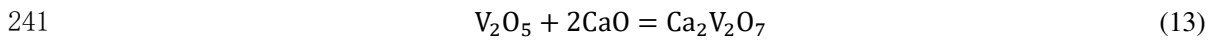
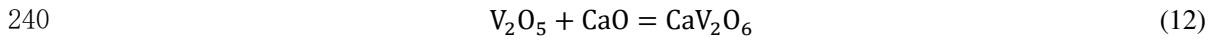
232 reported [6] as Eqs. (12)-(14). At the same time, the diffusion rate of Ca^{2+} is faster than that of V^{5+}

233 in the calcium vanadates as calculating in the following section. Thus, the reaction mechanism may

234 be that once the V-slag/CaO diffusion couple is heated to the reaction temperature, calcium

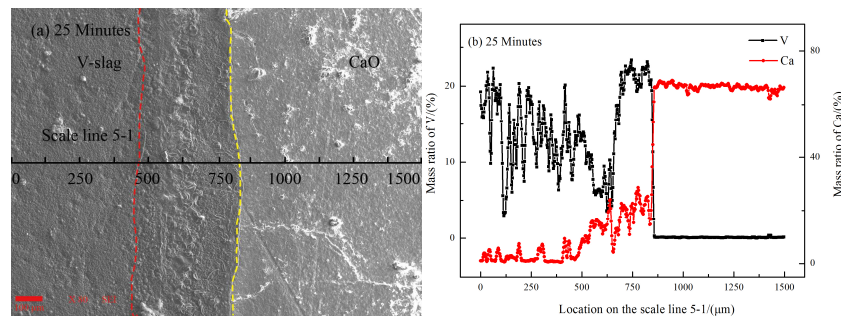
235 vanadates begin to form at the V_2O_5/CaO interface. Ca^{2+} diffuses toward V_2O_5 through Ca^{2+}
 236 vacancies, and holes (h) diffuse in the counter direction to maintain the electrical neutrality in the
 237 calcium vanadates. The diffused Ca^{2+} reacts with V_2O_5 to form calcium vanadates and generate
 238 holes at the calcium vanadates/ V_2O_5 interface as given in Eqs. (15)-(17).

239

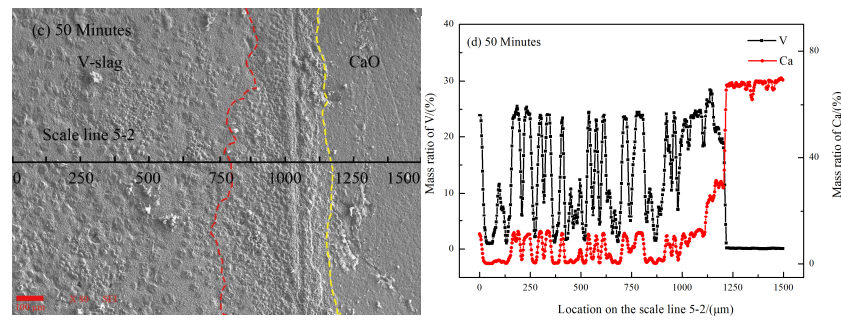


246

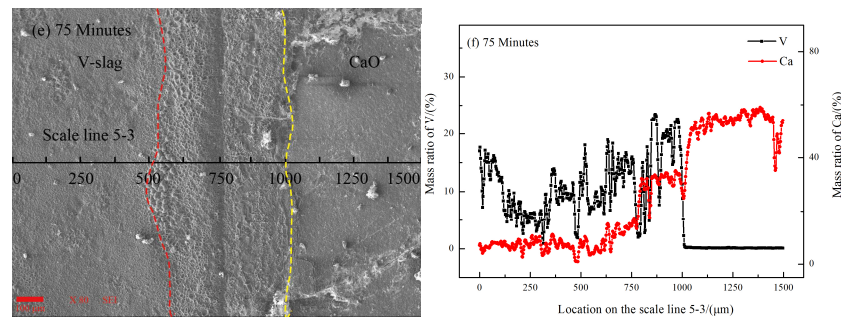
247

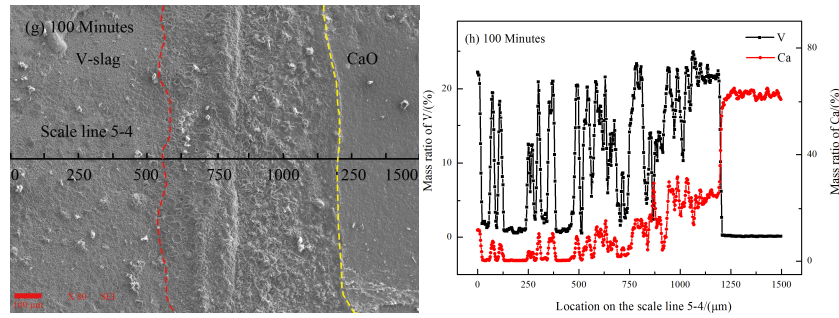


248



249



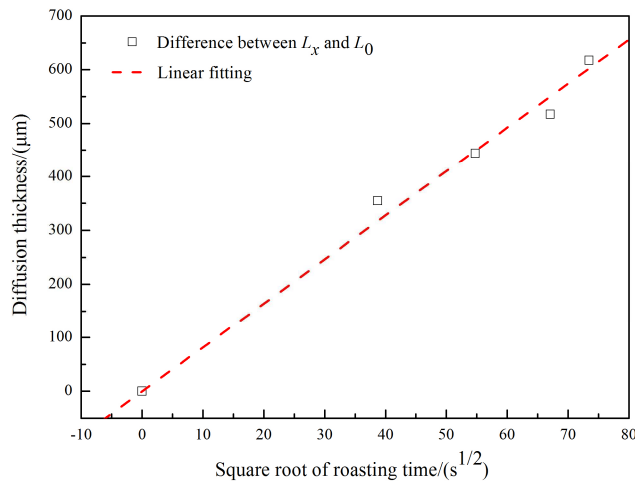


250

251 **Fig. 5.** Cross-sectional views and concentration profiles of the V-slag/CaO interface after annealing

252 at 1083 K in the air for different time.

253



254

255 **Fig. 6.** Relationship between the roasting time and the diffusion thickness at the diffusion surface

256 annealing at 1083 K in the air. The linear fitting coefficient of R^2 is 0.9965.

257

258 3.3. Evolution of the main generated compounds with the location at $S(xz)$

259

260 Fig. 7 is the phase diagram of the V_2O_5 -CaO system from 273 K to 3273 K calculated by the

261 FactSage. As thermodynamic predicting in Fig. 7, three new phases of CaV_2O_6 , $Ca_2V_2O_7$ and

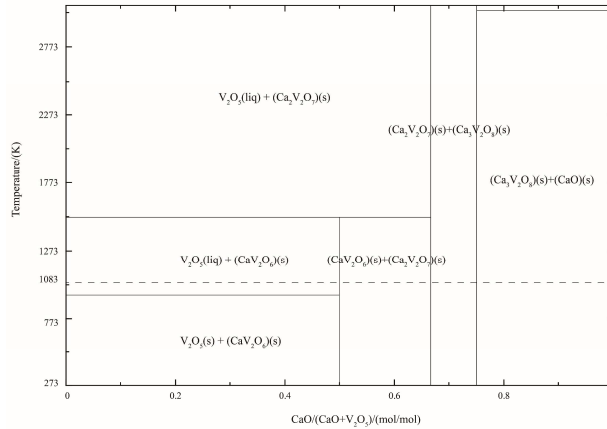
262 $Ca_3V_2O_8$ could be formed during annealing at 1083 K. The microscopic characteristics of the $S(xz)$

263 roasted for 75 minutes in the air are shown in Fig. 8(a). The enlarged drawings and EDS analysis of

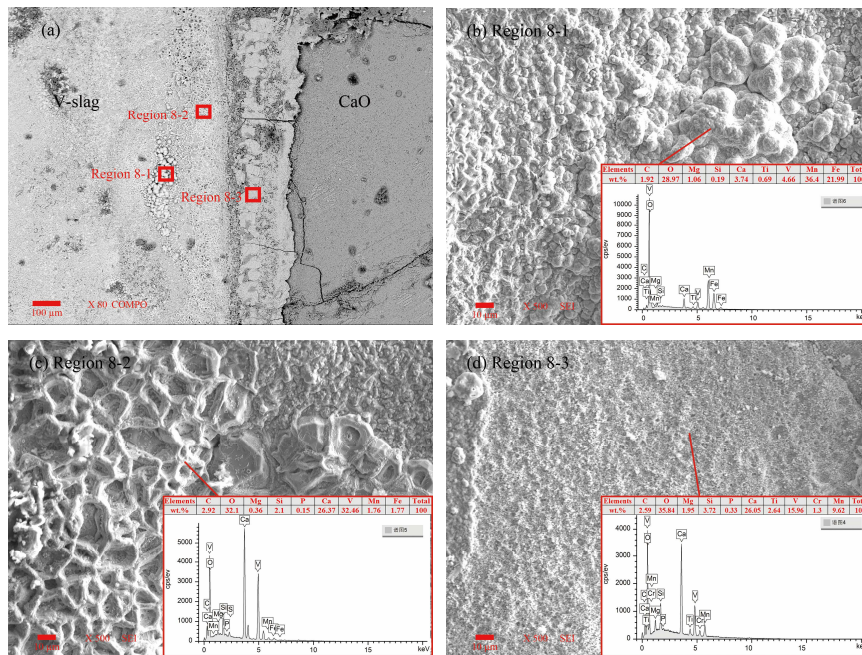
264 the generated compounds at different locations in Fig. 8(a) are shown in Fig. 8(b), Fig. 8(c), and

265 Fig. 8(d). As illustrated in Fig. 8(b), the spherical compounds are mainly composed of Mn, Fe, and
266 O with the total mass fraction accounting for 89.07 (regardless of the spraying C). According to the
267 reported XRD analysis [32,33], $(\text{Mn,Fe})(\text{V,Cr})_2\text{O}_4$ decomposed during the blank roasting of V-slag,
268 Fe was mainly gathered in Fe_2O_3 , Mn was enriched in $\text{Mn}_2\text{V}_2\text{O}_7$. In this case, region 8-1, where the
269 diffused Ca doesn't reach, can also be considered as a blank roasting area. However, the conclusion
270 of quantitative analysis (EDS) in Fig. 8(b) is not the same as the conclusion of qualitative analysis
271 (XRD) in the literature [32], namely, only a small amount of divalent Mn may be gathered into
272 $\text{Mn}_2\text{V}_2\text{O}_7$. Besides, another literature [6] reported that V_2O_5 was preferentially formed calcium
273 vanadates with Ca rather than manganese vanadates with Mn. Only the content of Ca was
274 insufficient could the excess V_2O_5 form manganese vanadates with the divalent Mn which was not
275 oxidized in advance by oxygen. Thus, it can be extracted from the literature [6] and the result in Fig.
276 8(b) that most of Mn should be preferentially enriched in manganese oxides. As shown in Fig. 8(c),
277 the generated compounds on the V-slag surface and near the V-slag/CaO interface have the bowl-
278 shaped appearance, and the main components are Ca, V, and O that account for 93.67 mass fraction
279 in total. If the oxygen occupied by SiO_2 , MgO , P_2O_5 , MnO_2 , and Fe_2O_3 are excluded, the chemical
280 formula of the generated compounds can be calculated as $\text{Ca}_{2.07}\text{V}_2\text{O}_{5.39}$ which may be the focal
281 calcium vanadate ($\text{Ca}_2\text{V}_2\text{O}_7$) as reported in the literature [6]. It is possible that not all oxides are
282 oxygen-saturated, which would cause too much oxygen has been excluded and lead to less oxygen
283 in $\text{Ca}_{2.07}\text{V}_2\text{O}_{5.39}$ than that in $\text{Ca}_2\text{V}_2\text{O}_7$. As shown in Fig. 8(d), the generated compounds on the CaO
284 surface and near the V-slag/CaO interface have no visible appearance, and the chemical formula is
285 calculated as $\text{Ca}_{4.14}\text{V}_2\text{O}_{9.45}$. The chemical formula can be split as $\text{Ca}_2\text{V}_2\text{O}_7 \cdot \text{Ca}_{2.14}\text{O}_{2.45}$ or
286 $\text{Ca}_3\text{V}_2\text{O}_8 \cdot \text{Ca}_{1.14}\text{O}_{1.45}$, which indicates the compounds consist of $\text{Ca}_2\text{V}_2\text{O}_7$ and CaO or $\text{Ca}_3\text{V}_2\text{O}_8$ and

287 CaO or the mixture of $\text{Ca}_2\text{V}_2\text{O}_7$, $\text{Ca}_3\text{V}_2\text{O}_8$ and CaO. This conclusion is consistent with the report
 288 [34] that if the temperature is higher than 1023 K and the content of CaO is sufficient, $\text{Ca}_2\text{V}_2\text{O}_7$ and
 289 $\text{Ca}_3\text{V}_2\text{O}_8$ may be generated during roasting the V-slag.
 290



291
 292 **Fig. 7.** Phase diagram of the V_2O_5 -CaO system calculated by FactSage using the Phase Diagram
 293 module.

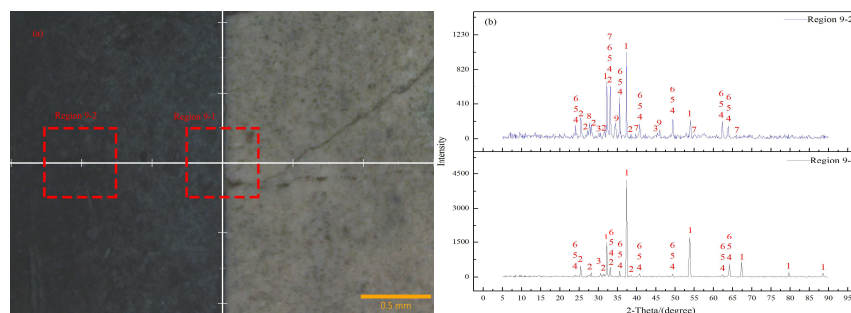


294
 295
 296 **Fig. 8.** Microscopic characteristics and EDS spectra of the generated compounds at different
 297 locations on the diffusion surface after annealing at 1083 K in the air for 75 minutes.
 298

299 The cross-sectional views of the diffusion interface annealed at 1083 K in the air for 75 minutes

300 are shown in Fig. 9(a), the crystal structures of the generated phases at the region 9-1 and region 9-
 301 2 are characterized by XRD, and the results are shown in Fig. 9(b). According to Fig. 9(b), the
 302 characteristic peaks of $\text{Ca}_3\text{V}_2\text{O}_8$ (JCPDS, 00-039-0090) and $\text{Ca}_2\text{V}_2\text{O}_7$ (JCPDS, 00-028-0836) are
 303 observed in the region 9-1, which verifies the EDS analysis in Fig. 8(c) and Fig. 8(d): the main
 304 generated compounds around the V-slag/CaO interface are $\text{Ca}_3\text{V}_2\text{O}_8$ and $\text{Ca}_2\text{V}_2\text{O}_7$. The diffraction
 305 peaks marked by 4,5 and 6 can be indexed to Fe_2O_3 (JCPDS, 01-089-0597) or $\text{Fe}_{1.8966}\text{Mg}_{0.1551}\text{O}_3$
 306 (JCPDS, 01-070-2674) or $\text{Fe}_9\text{TiO}_{15}$ (JCPDS, 00-054-1267). The characteristic peaks of Mn_2O_3
 307 (JCPDS, 03-065-7467) are presented in the region 9-2, which verifies the EDS analysis in Fig. 8(b):
 308 Mn^{2+} is oxidized into Mn_2O_3 at the V-slag surface where the diffused Ca has not reached. Besides,
 309 the diffraction peaks of $\text{CaMn}_7\text{O}_{12}$ (JCPDS, 01-084-0191) are shown in the region 9-2, and it
 310 suggests that some Mn_2O_3 react with CaO and generate $\text{CaMn}_7\text{O}_{12}$. The diffraction peaks of SiO_2
 311 (JCPDS, 01-079-1912) appears in the region 9-2, which is consistent with the results reported in the
 312 literature [32]. It should be noted that CaO (JCPDS, 01-070-4068) also appears in the region 9-2,
 313 which may be caused by the limitations of the analyzing equipment. When the 2-theta is 90° , the
 314 area of the scanning region (red borders in Fig. 9(a)) is $500\ \mu\text{m} \times 500\ \mu\text{m}$. When the 2-theta is less
 315 than 90° , the scanning area is greater than $500\ \mu\text{m} \times 500\ \mu\text{m}$, and the CaO surface is scanned.

316



317

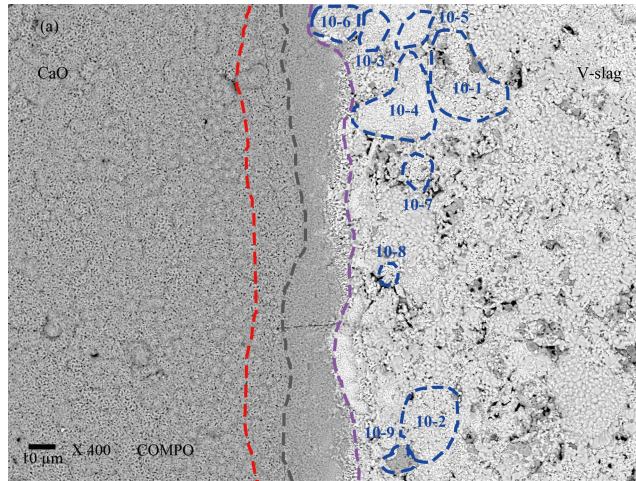
318

319 **Fig. 9.** The cross-sectional views captured by SmartLab (a) and the XRD patterns of the generated

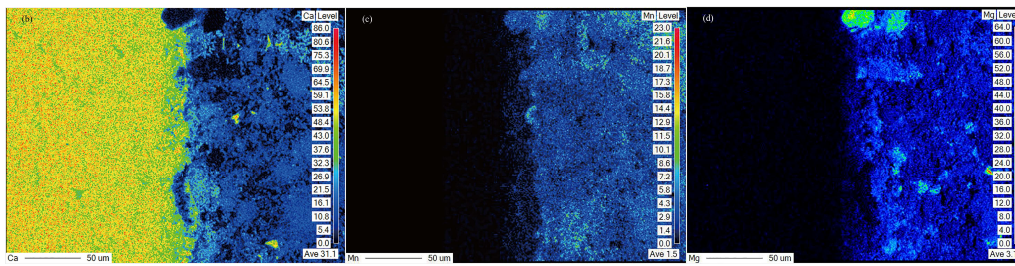
320 phases at different locations on the diffusion surface (b). 1-CaO; 2- $\text{Ca}_3\text{V}_2\text{O}_8$; 3- $\text{Ca}_2\text{V}_2\text{O}_7$; 4- Fe_2O_3 ;
321 5- $\text{Fe}_{1.8966}\text{Mg}_{0.1551}\text{O}_3$; 6- $\text{Fe}_9\text{TiO}_{15}$; 7- Mn_2O_3 ; 8- SiO_2 ; 9- $\text{CaMn}_7\text{O}_{12}$.

322

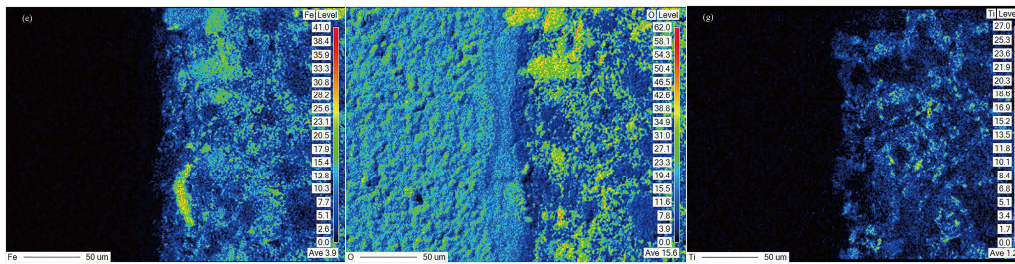
323 Fig. 10 shows the cross-sectional views and the elemental maps of the diffusion interface
324 annealed at 1083 K for 5 minutes in the air. The diffusion boundaries marked as the purple dotted
325 curve and the red dotted curve in Fig. 10(a) were determined by the Ca map in Fig. 10(b) and V map
326 in Fig. 10(h). It can be extracted from the EDS analysis that Fe does not diffuse to the CaO surface.
327 Thus, the original interface between V-slag and CaO can be determined by the Fe map in Fig. 10(e)
328 and marked as the gray dotted curve in Fig. 10(a). It can be seen from the three diffusion boundaries
329 that Ca^{2+} diffuses faster than V^{5+} in the generated compounds. As shown in Fig. 10(a), Fig. 10(c),
330 and Fig. 10(h), the regions (region 10-1, region 10-2, and region 10-3) containing primary Mn are
331 only distributed of little V, which confirms the conclusion obtained from the EDS and XRD analysis
332 that most of Mn is enriched into Mn_2O_3 instead of manganese vanadates. As shown in Fig 10(a),
333 Fig. 10(d), Fig. 10(e), and Fig. 10(f), the phase of region 10-4 mainly consists of Fe and O, it should
334 be Fe_2O_3 . The phase of region 10-5 mainly consists of Mg, Fe, and O, and it may be
335 $\text{Fe}_{1.8966}\text{Mg}_{0.1551}\text{O}_3$. The phase of region 10-6 mainly consists of Mg and O, and it should be MgO.
336 As shown in Fig. 10(a), Fig. 10(h), and Fig. 10(i), the region 10-7 and region 10-8 contain Cr but
337 do not contain Ca or V. It indicates that Cr is at a disadvantage compared with V when occupying
338 the original Ca in the V-slag, which is consistent with the conclusion in the literature [34]. As shown
339 in Fig. 10(a), Fig. 10(f), and Fig. 10(j), the phase of region 10-9 mainly consists of Si and O, and it
340 may be SiO_2 .



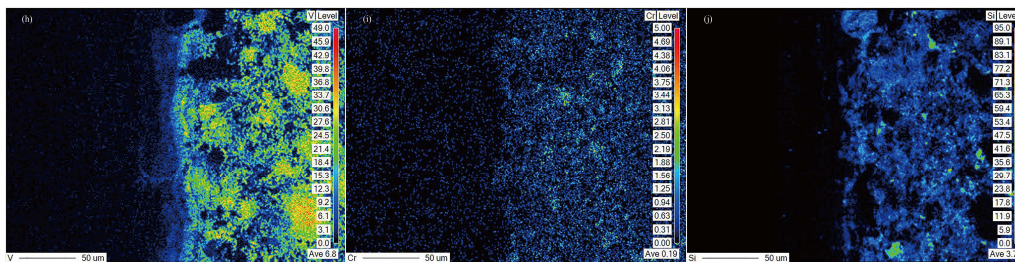
341



342



343



344

345 **Fig. 10.** Cross-sectional views and elements maps of the diffusion interface roasted at 1083 K for 5
 346 minutes in the air.

347

348 **3.4. Interdiffusion coefficients of Ca^{2+} and V^{5+} in the calcium vanadates**

349

350 The black solid points in Fig. 11(a) are the raw data of the Ca concentration profiles obtained

351 by EPMA on the scale line 5-3 in Fig. 5. The red and green histograms in Fig. 11(a) are the
352 concentration differences in Eq. (6) and Eq. (7), respectively. The areas (A_{afh} and A_{efj} in Fig. 3) at a
353 location can be calculated as the sum of the areas of the histograms, i.e., the sum of the concentration
354 difference times the scanning step of 2.5 μm . A_{afh} and A_{efj} are shown in Fig. 11(b), and they are
355 closest at 797.5 μm on the scale line 5-3, which indicates 797.5 μm on the scale line 5-3 is the
356 Matano surface. Subsequently, the new X -axis is established with origin of 797.5 μm on the scale
357 line 5-3. A_{hbgf} in Fig. 3(d) is calculated as the product of the concentration difference in Fig. 11(a)
358 and the coordinate on the X -axis, and the data are shown in Fig. 11(c). Finally, A_{abgf} in the
359 Boltzmann-Matano method can be calculated by Eq. (8) and constructed in Fig. 11(d). The slopes
360 of the raw data of the Ca concentration profiles in Fig. 11(a) are calculated by Eq. (9) and Eq. (10)
361 and plotted in Fig. 11(e). If the Ca concentration curve is monotonic, the slopes should all be positive
362 as the concentration increasing with the increase of the coordinates. However, the calculated results
363 show that the slopes in some intervals are negative. Here, the average of the two positive slopes at
364 both ends of the interval is used to replace the negative slopes in the interval. The interdiffusion
365 coefficients of Ca^{2+} ($D_{\text{Ca}^{2+}}$) as a function of the molar fraction of Ca are calculated by Eq. (11) and
366 presented in Fig. 11(f). The $D_{\text{Ca}^{2+}}$ in the generated compounds are substantially in the orders of
367 magnitudes of 10^{-9} to 10^{-7} $\text{cm}^2 \cdot \text{s}^{-1}$. If the profiles in Fig. 11(a) are strictly increasing with coordinates,
368 the A_{abgf} in Fig. 11(d) and slope in Fig. 11(e) should increase first and then decrease as the coordinate
369 increasing. However, the volatility of the raw data in Fig. 11(a) causes the fluctuations of the A_{abgf}
370 in Fig. 11(d) and the slope in Fig. 11(e), which also affect the calculated $D_{\text{Ca}^{2+}}$ in Fig. 11(f). As usual,
371 the average of the interdiffusion coefficients in a certain concentration interval was proposed to
372 express the diffusion ability [35-37]. In this case, the average of $D_{\text{Ca}^{2+}}$ with the Ca molar fraction of

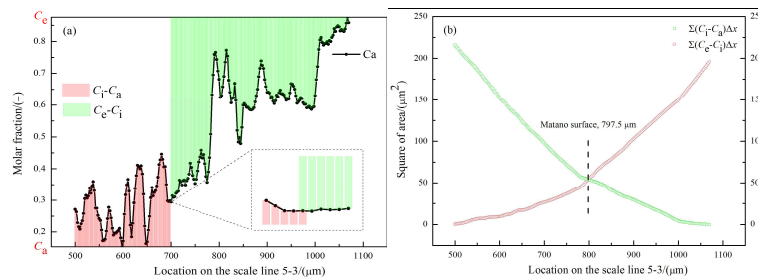
373 0.15-0.86 is calculated as $2.54 \times 10^{-8} \text{ cm}^2 \cdot \text{s}^{-1}$. Besides, the average of $D_{\text{Ca}^{2+}}$ calculated by Eq. (11)
374 and the other method [24, 38-40] provided in the literature are listed in Table 2. As given in Table
375 2, the average of $D_{\text{Ca}^{2+}}$ calculated by Eq. (11) is in agreement with that calculated by the method
376 reported in the literature [38]. At the same time, the average of $D_{\text{Ca}^{2+}}$ in the calcium vanadates is
377 also in the same order of magnitude as that in the $\text{Ca}_2\text{Fe}_2\text{O}_5$ [24]. These results indicate that the
378 method of calculating the interdiffusion coefficient in this paper is reliable. Similarly, the data
379 generated during the calculation of the interdiffusion coefficients using the V concentration profiles
380 are plotted in Fig. 12. The average of the interdiffusion coefficients of V^{5+} with the V molar fraction
381 of 0.001 to 0.43 is $1.96 \times 10^{-8} \text{ cm}^2 \cdot \text{s}^{-1}$. It can be extracted from the calculated results that the diffusion
382 of Ca^{2+} is faster than the diffusion of V^{5+} in the calcium vanadates, and the calcium vanadates are
383 mainly formed on the V-slag surface. Thus, when roasting the V-slag powders with CaO powders,
384 the particle size of the V-slag should be greater than that of CaO.

385 **Table 2**

386 Interdiffusion coefficients of Ca^{2+} calculated in the present work and the literature [24,38]

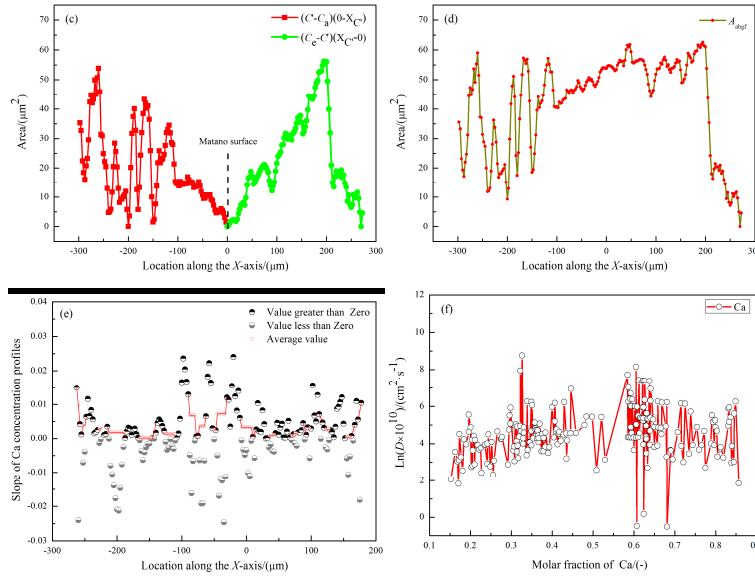
Condition	System	Profiles	Method	Medium	D_{average}
1083 K	V-slag/CaO	Fig. 5(f)	Eq. (11)	$\text{Ca}_2\text{V}_2\text{O}_7$, $\text{Ca}_3\text{V}_2\text{O}_8$	$2.54 \times 10^{-8} \text{ cm}^2 \cdot \text{s}^{-1}$
1083 K	V-slag/CaO	Fig. 5(f)	Reference [38]	$\text{Ca}_2\text{V}_2\text{O}_7$	$5.2 \times 10^{-8} \text{ cm}^2 \cdot \text{s}^{-1}$
1173 K	CaO/FeO	Reference [24]	Reference [24]	$\text{Ca}_2\text{Fe}_2\text{O}_5$	$2.0 \times 10^{-8} \text{ cm}^2 \cdot \text{s}^{-1}$

387



388

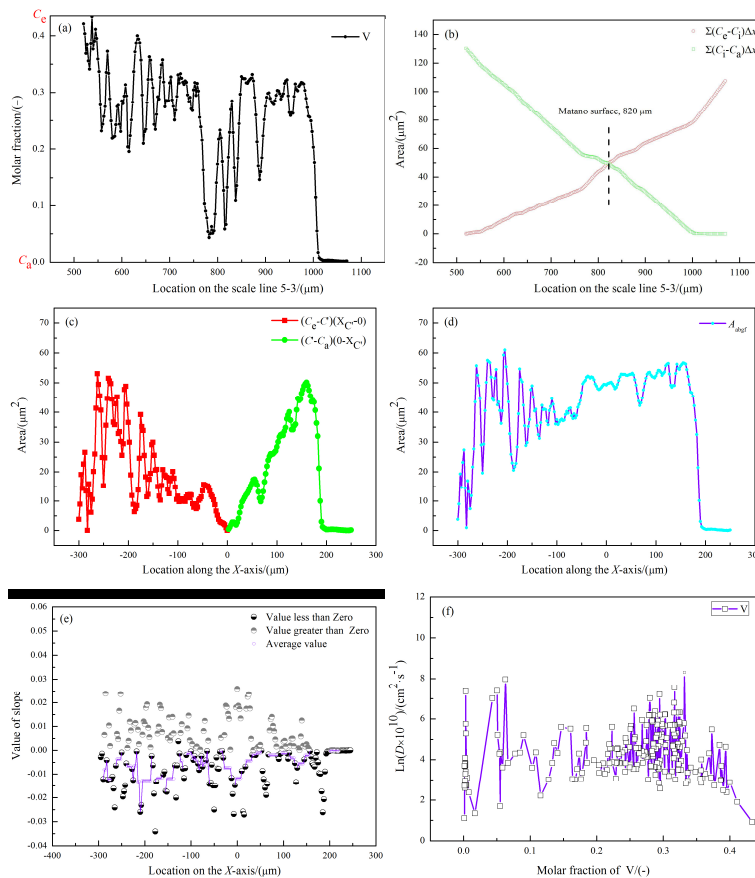
389



390

391 **Fig. 11.** Calculated data of determining the Matano surface, integral, differential, and the
 392 interdiffusion coefficient by the concentration profiles of Ca.

393



394

395

396 **Fig. 12.** Calculated data of determining the Matano surface, integral, differential, and the
 397 interdiffusion coefficient by the concentration profiles of V.

398

399 **4. Conclusion**

400

401 In this paper, the V-slag/CaO diffusion couple was prepared by the vacuum hot-pressing
402 method, and the diffusion experiment was carried out at 1083 K in the air in the muffle furnace.

403 Although the V-slag/CaO diffusion couple can be assembled by the method in this paper, it will start
404 cracking after being stored in a vacuum oven for 1-2 weeks. Therefore, the key to study the diffusion
405 couple containing CaO is to prepare the diffusion couple that will not crack at high temperatures
406 and not deliquesce at low temperatures. Also, the concentration profiles on the V-slag surface are
407 too fluctuant to directly apply in the Boltzmann-Matano method to calculate the interdiffusion
408 coefficient. In this paper, a new method is proposed to determine the Matano surface and calculate
409 the interdiffusion coefficients without smoothing the concentration profiles. According to the result
410 of this paper and related literature, the following conclusions can be used as a reference for the
411 readers.

412 1. The diffusion thickness of the calcium vanadates is generally proportional to the square root
413 of the roasting time.

414 2. At the V-slag surface where the diffused Ca has not reached, Fe and Mn are mainly enriched
415 in the corresponding oxides after decomposing from the spinels. The low-valent V is oxidized and
416 reacted with the original Ca in the V-slag to form $\text{Ca}_2\text{V}_2\text{O}_7$. Cr is at a disadvantage of occupying the
417 original Ca in the V-slag comparing with V.

418 3. At the V-slag surface where the diffused Ca is already reached, the main generated phase is
419 $\text{Ca}_2\text{V}_2\text{O}_7$.

420 4. At the CaO surface, the main generated phases may be the combination of $\text{Ca}_2\text{V}_2\text{O}_7$ and
421 $\text{Ca}_3\text{V}_2\text{O}_8$.

422 5. The diffusion coefficient of Ca^{2+} in calcium vanadates is greater than that of V^{5+} , which
423 indicates that calcium vanadates are mainly formed on the V-slag surface. Thus, the size of the V-
424 slag particle should be larger than that of CaO particle in the practice roasting.

425

426 **Acknowledgment**

427 This work was financially supported by the National Science Foundation of China (Nos.
428 51674084 and U1502273) and the Fundamental Research Funds for the Central Universities (No.
429 182503035).

430

431 **Reference**

432 [1] H.Y. Li, H.X. Fang, K. Wang, W. Zhou, Z. Yang, X.M. Yan, W.S. Ge, Q.W. Li, B. Xie,

433 Asynchronous extraction of vanadium and chromium from vanadium slag by stepwise

434 sodium roasting-water leaching, *Hydrometallurgy* 156 (2015) 124-135.

435 <https://doi.org/10.1016/j.hydromet.2015.06.003>

436 [2] W.C. Song, K. Li, Q. Zheng, H. Li, A novel process of vanadium extraction from molten

437 vanadium bearing slag, *Waste Biomass Valori.* 5(3) (2014) 327-332.

438 <https://doi.org/10.1007/s12649-013-9286-z>

439 [3] A.J. Teng, X.X. Xue, A novel roasting process to extract vanadium and chromium from high

440 chromium vanadium slag using a NaOH- NaNO_3 binary system, *J. Hazardous Mater.* 379

441 (2019). <https://doi.org/10.1016/j.jhazmat.2019.120805>

442 [4] Y.L. Ji, S.B. Shen, J.H. Liu, Y. Xue, Cleaner and effective process for extracting vanadium

443 from vanadium slag by using an innovative three-phase roasting reaction, *J. Clean. Prod.* 149

444 (2017) 1068-1078. <https://doi.org/10.1016/j.jclepro.2017.02.177>

445 [5] E.I.L. Silva, A. Shimizu, H. Matsunami, Salt pollution in a Japanese stream and its effects on

446 water chemistry and epilithic algal chlorophyll-a, *Hydrobiologia* 437(1-3) (2000) 139-148.
447 <https://doi.org/10.1023/a:1026598723329>

448 [6] J.H. Zhang, W. Zhang, L. Zhang, S.Q. Gu, Mechanism of vanadium slag roasting with calcium
449 oxide, *Int. J. Miner. Process.* 138 (2015) 20-29. <https://doi.org/10.1016/j.minpro.2015.03.007>

450 [7] P. Cao, X.L. Yang, Y. Peng, Z.B. Fu, L. Chen, Research on the mechanism of producing
451 calcium vanadate, *Advanced Materials Research* 581-582 (2012) 996-1001. [https://doi.org/](https://doi.org/10.4028/www.scientific.net/AMR.581-582.996)
452 [10.4028/www.scientific.net/AMR.581-582.996](https://doi.org/10.4028/www.scientific.net/AMR.581-582.996)

453 [8] J.H. Zhang, W. Zhang, Z.L. Xue, Oxidation kinetics of vanadium slag roasting in the presence
454 of calcium oxide, *Min. Proc. Ext. Met. Rev.* 38(5) (2017) 265-273.
455 <https://doi.org/10.1080/08827508.2017.1289197>

456 [9] C.J. Li, Z.J. Yuan, R. Guo, W.D. Xuan, Z.M. Ren, Y.B. Zhong, X. Li, H. Wang, Q.L. Wang,
457 Reaction diffusion in Ni-Al diffusion couples in steady magnetic fields, *J. Alloy. Comp.* 641
458 (2015) 7-13. <https://doi.org/10.1016/j.jallcom.2015.04.061>

459 [10] Z.S Ren, X.J. Hu, X.X. Xue, K.C. Chou, Solid state reaction studies in Fe₃O₄-TiO₂ system by
460 diffusion couple method, *J. Alloy. Comp.* 580 (2013) 182-186.
461 <https://doi.org/10.1016/j.jallcom.2013.05.114>

462 [11] Y. Zhou, Q.Wang, D.L.Sun, X.L.Han, Co-effect of heat and direct current on growth of
463 intermetallic layers at the interface of Ti-Ni diffusion couples, *J. Alloy. Comp.* 509 (2011)
464 1201-1205. <https://doi.org/10.1016/j.jallcom.2010.09.182>

465 [12] I.B. Bashir, Mechanisms of densification during the hot pressing of calcium oxide and
466 synthetic dolomite, *Material Science & Engineering* 61(1) (1983) 51-57.
467 [https://doi.org/10.1016/0025-5416\(83\)90125-8](https://doi.org/10.1016/0025-5416(83)90125-8)

- 468 [13] M. Peiteado, A.C. Caballero, D. Makovec, Diffusion and reactivity of ZnO-MnO_x system, J.
469 Solid State Chem. 180(9) (2007) 2459-2464. <https://doi.org/10.1016/j.jssc.2007.07.001>
- 470 [14] K.P. Chao, P. Wang, Y.T. Wang, Diffusion and solubility coefficients determined by
471 permeation and immersion experiments for organic solvents in HDPE geomembrane, J.
472 Hazardous Mater. 142 (2007) 227-235. <https://doi.org/10.1016/j.jhazmat.2006.08.022>
- 473 [15] C. Matano, On the relation between the diffusion-coefficients and concentrations of solid
474 metals (the nickel-copper system), Jpn. J. Phys. 8 (1993), 109-113.
- 475 [16] A. Fick, Ueber diffusion, Ann. Phys. 170 (1855) 59-86.
476 <https://doi.org/10.1002/andp.18551700105>
- 477 [17] L. Boltzmann, Zur Integration der diffusionsgleichung bei variablen diffusions-coefficienten,
478 Ann. Phys. 289 (1894) 959-964. <https://doi.org/10.1002/andp.18942891315>
- 479 [18] P.J. Tumidajski, G.W. Chan, R.F. Feldman, G. Strathdee, A Boltzmann-Matano analysis of
480 chloride diffusion, Cement Concrete Res. 25(7) (1995) 1556-1566.
481 [https://doi.org/10.1016/0008-8846\(95\)00149-7](https://doi.org/10.1016/0008-8846(95)00149-7)
- 482 [19] M.A. Dayananda, Determination of eigenvalues, eigenvectors, and interdiffusion coefficients
483 in ternary diffusion from diffusional constraints at the Matano plane, Acta Mater. 129 (2017)
484 474-481. <https://doi.org/10.1016/j.actamat.2017.03.012>
- 485 [20] M. Appel, Solution for Fick's 2nd law with variable diffusivity in a multi-phase system, Scr.
486 Metall. 2(4) (1967) 217-221. [https://doi.org/10.1016/0036-9748\(68\)90231-7](https://doi.org/10.1016/0036-9748(68)90231-7)
- 487 [21] C. Wagner, The evaluation of data obtained with diffusion couples of binary single-phase and
488 multiphase systems, Acta Metall. 17(2) (1969) 99-107. [https://doi.org/10.1016/0001-](https://doi.org/10.1016/0001-6160(69)90131-X)
489 [6160\(69\)90131-X](https://doi.org/10.1016/0001-6160(69)90131-X)

- 490 [22] C. Heiligers, C.J. Pretorius, J.H. Neethling, Interdiffusion of hafnium carbide and titanium
491 carbide during hot-pressing, *Int. J. Refract. Met. H.* 31 (2012) 51-55.
492 <https://doi.org/10.1016/j.ijrmhm.2011.09.005>
- 493 [23] H.R Yue, X.X Xue, China Patent, No.CN110263292A (2019).
- 494 [24] H. Fukuyama, K. Hossain, K. Nagata, Solid-state reaction kinetics of the system CaO-FeO,
495 *Metall. Mater. Trans. B* 33(2) (2002) 257-264. <https://doi.org/10.1007/s11663-002-0010-9>
- 496 [25] W.W. Sun, H. Ehteshami, P.R.C. Kent, P.A. Korzhavyi, Self-diffusion of Ti interstitial based
497 point defects and complexes in TiC, *Acta Mater.* 165 (2019) 381-387.
498 <https://doi.org/10.1016/j.actamat.2018.11.056>
- 499 [26] X.W. Zhou, R.E. Jones, J. Gruber, Molecular dynamics simulations of substitutional
500 diffusion, *Comp. Mater. Sci.* 128 (2017) 331-336.
501 <https://doi.org/10.1016/j.commatsci.2016.11.047>
- 502 [27] Z.P. Lin, L.L. Bai, X. Zhang, H.F. Dong, F.G. Wu, Na-vacancies-induced magnetism in
503 Na_xMnO_2 , *J. Magn. Magn. Mater.* 468 (2018) 164-167.
504 <https://doi.org/10.1016/j.jmmm.2018.08.009>
- 505 [28] K.N. Goswami, A. Mottura, A kinetic monte carlo study of vacancy diffusion in non-dilute
506 Ni-Re alloys, *Mat. Sci. Eng. A-Struct.* 743 (2019) 265-273.
507 <https://doi.org/10.1016/j.msea.2018.11.064>
- 508 [29] Z.S. Mi, L. Chen, C.M. Shi, Y. Ma, D.C. Wang, X.L. Li, H.M. Liu, L.J. Qiao, The effects of
509 strain and vacancy defects on the electronic structure of Cr_2O_3 , *Comp. Mater. Sci.* 144 (2018)
510 64-69. <https://doi.org/10.1016/j.commatsci.2017.12.012>
- 511 [30] K.J. Relmasira, A.Yu. Leonov, P.I. Malenko, Application of molecular dynamics method for

512 simulation of the process of increasing the diffusion mobility, *Procedia Engineering* 206
513 (2017) 636-641. <https://doi.org/10.1016/j.proeng.2017.10.529>

514 [31] S.A. Kislenko, M.S. Vlaskin, A.Z. Zhuk, Diffusion of cation impurities by vacancy
515 mechanism in α -Al₂O₃: Effect of cation size and valence, *Solid State Ionics* 293 (2016) 1-6.
516 <https://doi.org/10.1016/j.ssi.2016.05.021>

517 [32] X.F. Zhang, F.G. Liu, X.X. Xue, T. Jiang, Effects of microwave and conventional blank
518 roasting on oxidation behavior, microstructure and surface morphology of vanadium slag
519 with high chromium content, *J. Alloy. Compd.* 686 (2016) 356-365.
520 <https://doi.org/10.1016/j.jallcom.2016.06.038>

521 [33] X.S. Li, B. Xie, Extraction of vanadium from high calcium vanadium slag using direct
522 roasting and soda leaching, *Int. J. Min. Met. Mater.* 19(7) (2012) 595-601.
523 <https://doi.org/10.1007/s12613-012-0600-8>

524 [34] T. Jiang, J. Wen, M. Zhou, X.X. Xue, Phase evolutions, microstructure and reaction
525 mechanism during calcification roasting of high chromium vanadium slag, *J. Alloy. Compd.*
526 742 (2018), 402-412. <https://doi.org/10.1016/j.jallcom.2018.01.201>

527 [35] L.R. Ram-Mohan, M.A. Dayananda, A transfer matrix method for the calculation of
528 concentrations and fluxes in multicomponent diffusion couples, *Acta Mater.* 54(9) (2006)
529 2325-2334. <https://doi.org/10.1016/j.actamat.2006.01.021>

530 [36] P. Zhang, T. Debroy, S. Seetharaman, Interdiffusion in the MgO-Al₂O₃ spinel with or without
531 some dopants, *Metall. Mater. Trans. A* 27(8) (1996) 2105-2114.
532 <https://doi.org/10.1007/BF02651865>

533 [37] Y. Yuan, Y.Y. Guan, D.J. Li, N. Moelans, Investigation of diffusion behavior in Cu-Sn solid

534 state diffusion couples, *J. Alloy. Comp.* 661 (2016) 282-293.
535 <https://doi.org/10.1016/j.jallcom.2015.11.214>

536 [38] K. Kawamura, A. Saiki, T. Maruyama, K. Nagata, Diffusion coefficient of yttrium ion in
537 YCrO_3 , *J. Electrochem. Soc.* 142(9) (1995), 3073-3077. <https://doi.org/10.1149/1.2048690>

538 [39] C. Wagner, Investigations on silver sulfide, *J. Chem. Phys.* 21(10) (1953) 1819-1827.
539 <https://doi.org/10.1063/1.1698670>

540 [40] T. Maruyama, K. Kawamura, A. Saiki, K. Nagata, Thermodynamics and diffusivity of yttrium
541 in yttrium chromite (YCrO_3), *Key. Eng. Mater.* 111-112 (1995) 303-320.
542 <https://doi.org/10.4028/www.scientific.net/kem.111-112.30>

543
544
545
546
547
548
549
550
551
552
553
554
555

556 Appendix

557 The meaning of the symbols are listed in Table A1.

558

559

Table A1. Descriptions of the mainly symbols

S	Surface
$S(xz)$	Surface parallel to the x -axis and z -axis
x	Location on the x -axis
x_a	Location of initial concentration
x_e	Location of initial concentration
x_m	Location of Matano surface
X	Location on the X -axis
X'	Location at a particular concentration
C	Concentration
C_a	Initial concentration
C_e	Initial concentration
C_m	Concentration of Matano surface
C'	Concentration at a particular location
$C_{X'-2\Delta X}$	Concentration at $X'-2\Delta X$
$C_{X'-\Delta X}$	Concentration at $X'-\Delta X$
$C_{X'+\Delta X}$	Concentration at $X'+\Delta X$
$C_{X'+2\Delta X}$	Concentration at $X'+2\Delta X$
A	Area
A_{abgf}	Area enclosed by points a, b, g, and f
A_{abm}	Area enclosed by points a, b, and m
A_{dem}	Area enclosed by points d, e, and m
A_{afh}	Area enclosed by points a, f, and h
A_{efj}	Area enclosed by points e, f, and j
A_{hbgf}	Area enclosed by points h, b, g, and f
D	Interdiffusion coefficient
$D_{average}$	Average of interdiffusion coefficient
k	Slope
L_0	Diffusion thickness before roasting
L_x	Diffusion thickness after roasting on the x -axis
t	Time

560

561 Relative error of the calculated interdiffusion coefficient (σ_D/D).

562 The following Eq.(A1) is deduced from the logarithm of the Boltzmann-Matano formula. According

563 to Eq. (A2) and the propagation of error. The relative error of D can be expressed by the relative

564 errors of A and k in Eq. (A3) and Eq. (A4), where the relative error of time is assumed to be zero.
565 According to Eq. (8) and the propagation of error, Eq. (A5) and Eq. (A6) are proposed to calculate
566 the relative error of A . In the sight of Eq. (9) and Eq. (10), the relative error of k can be described
567 by Eq. (A7) and Eq. (A8). Finally, the relative error of D can be calculated as the function of the
568 relative error of C (0.01) as given in Eq. (A9). The relative errors of D at different concentrations
569 are constructed in Fig. A1. In Fig. A1, the relative errors increase sharply as the concentrations
570 closing to the initial concentrations. When the concentrations reach the initial concentrations
571 gradually, the concentration gradient gradually decreases to zero, which lead to the sharply increasing
572 of the relative errors in Eq. (A9). The relationship between the relative error and concentration
573 reflects the limitation of the calculating method in the present work, that is, the calculated
574 interdiffusion coefficients closed to the initial concentrations may have large relative errors.

$$575 \quad \ln D = \ln\left(-\frac{1}{2t} \frac{A}{k}\right) \quad (\text{A1})$$

$$576 \quad \frac{\sigma_D}{D} \approx \frac{dD}{D} = d \ln D \quad (\text{A2})$$

$$577 \quad \frac{\sigma_D}{D} = \left| -\frac{1}{2t} \frac{A}{k} \right| \left(\left| -\frac{1}{2t} \frac{1}{k} \right| \sigma_A + \left| \frac{A}{2t} \frac{1}{k^2} \right| \sigma_k \right) \quad (\text{A3})$$

$$578 \quad \frac{\sigma_D}{D} = \frac{\sigma_A}{|A|} + \frac{\sigma_k}{|k|} \quad (\text{A4})$$

$$579 \quad \sigma_A = \begin{cases} \Delta X \left| \frac{X_f - X_a}{\Delta X} \right| (\sigma_C + |-1| \sigma_C) + |X_f| (\sigma_C + |-1| \sigma_C), & X < 0 \\ \Delta X \left| \frac{X_e - X_f}{\Delta X} \right| (\sigma_C + |-1| \sigma_C) + |X_f| (\sigma_C + |-1| \sigma_C), & X > 0 \end{cases} \quad (\text{A5})$$

$$580 \quad \sigma_A = \begin{cases} -2X_a \sigma_C, & X < 0 \\ 2X_f \sigma_C, & X > 0 \end{cases} \quad (\text{A6})$$

581 For interior points:

$$582 \quad \sigma_k = \frac{1}{12\Delta X} (\sigma_C + |-8| \sigma_C + 8\sigma_C + |-1| \sigma_C) = \frac{3}{2\Delta X} \sigma_C \quad (\text{A7})$$

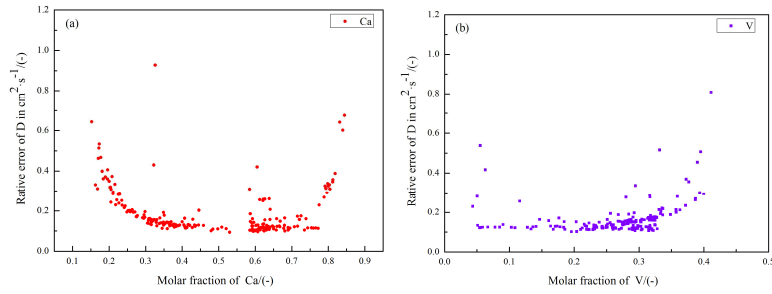
583 For end-points:

$$584 \quad \sigma_k = \frac{1}{12\Delta X} (|-25| + 48\sigma_C + |-36| \sigma_C + 16\sigma_C + |-3| \sigma_C) = \frac{32}{3\Delta X} \sigma_C \quad (\text{A8})$$

585

586

$$\frac{\sigma_D}{D} = \begin{cases} \frac{-2X_a\sigma_C}{|A|} + \frac{3}{2\Delta X}\frac{\sigma_C}{|k|}, & X < 0, \text{interior points} \\ \frac{2X_f\sigma_C}{|A|} + \frac{3}{2\Delta X}\frac{\sigma_C}{|k|}, & X > 0, \text{interior points} \\ \frac{-2X_a\sigma_C}{|A|} + \frac{32}{3\Delta X}\frac{\sigma_C}{|k|}, & X < 0, \text{end - points} \\ \frac{2X_f\sigma_C}{|A|} + \frac{32}{3\Delta X}\frac{\sigma_C}{|k|}, & X > 0, \text{end - points} \end{cases} \quad (\text{A9})$$



587

588 Fig. A1. Relative errors of the calculated Ca^{2+} interdiffusion coefficients and V^{5+} interdiffusion

589 coefficients.